

Characterization and integration of a new oxidative flow reactor for use in *in vitro* and human exposure systems with diesel exhaust and other aerosol

Vikram Choudhary¹, Yu Xi¹, Cynthia Pham², Yuetong Zhang², Kristen Hardy, Christopher F Rider¹, Julia Zaks³, Allan K. Bertram³, Arthur Chan⁴, William H. Brune⁵*, Chris Carlsten¹*

¹Air Pollution Exposure Laboratory, Division of Respiratory Medicine, Department of Medicine, Vancouver Coastal Health Research Institute, The University of British Columbia, British Columbia, Vancouver, V5Z1W9, Canada

²Department of Mechanical Engineering, The University of British Columbia, British Columbia, Vancouver, V6T1Z4, Canada

³Department of Chemistry, The University of British Columbia, British Columbia, Vancouver, V6T1Z1, Canada

⁴Department of Chemical Engineering and Applied Chemistry, University of Toronto, Ontario, M5S3E5, Canada

⁵Department of Meteorology and Atmospheric Science, College of Earth and Mineral Sciences, The Pennsylvania State University, Pennsylvania, 16802, USA

*Corresponding authors: William H. Brune (whb2@psu.edu); Chris Carlsten (carlsten@mail.ubc.ca)

Abstract

Freshly emitted air pollutants may not represent real-world exposure conditions in human studies, especially for communities exposed to aged air pollutants. This study presents the design and characterization of a new oxidative flow reactor (OFR), named the Fast-oxidation Box (FoxBox, volume of 1019 L). Our aim is to simulate atmospheric aging of diesel exhaust (DE) with this system for cellular (*in vitro*) and controlled human studies, a unique capability globally. We measured: (a) residence time distribution (RTD) for DE-derived CO₂, SO₂, and particles, (b) DE particle transmission efficiency, (c) low-volatility organic compounds (LVOC) losses, and (d) particle size distribution, secondary organic aerosol (SOA) formation, and aerosol mass spectra of DE during photochemical oxidation (from OH exposure of $(1.9 \text{ to } 9.5) \times 10^{11} \text{ molec cm}^{-3} \text{ s}$). Our results demonstrate turbulent flow-like conditions in FoxBox with narrower RTD for particles than gases. The particle transmission efficiency was nearly 100% for mobility diameters between 15 and 615 nm. LVOC losses to FoxBox walls were minimal. The changes in particle size distributions (e.g., formation of ultrafine particles) and chemical composition (e.g., SOA formation, increased O:C, etc.) during photochemical oxidation in FoxBox were like those observed in the atmosphere and other OFRs. Our preliminary study on cell viability found that photochemical oxidation significantly reduced cell viability, supporting observations that communities distant from air pollution sources are affected and vulnerable. The controlled human exposures with more realistic aerosol characteristics, such as those produced by FoxBox, may provide critical insight in this regard that has been lacking to date.

Keywords: Residence time distribution, particle transmission efficiency, diesel exhaust, low-volatile organic compounds, secondary organic aerosol, photochemical oxidation, cell viability.

1. Introduction

Aerosol are fundamental to air pollution and have a significant impact on Earth's climate and public health. Aerosol perturb the Earth's climate system by scattering and absorption of solar and terrestrial radiation. They also act as cloud condensation nuclei (CCN) and ice nuclei, affecting the lifetime and precipitation of clouds. Increasing evidence from epidemiological and toxicological research indicates that global exposure to atmospheric air pollution, especially PM_{2.5} (particulate matter with aerodynamic diameter $\leq 2.5 \mu\text{m}$), has increased by 20% between 1990 and 2013 (Brauer et al. 2016), and is strongly linked with adverse health outcomes such as respiratory and cardiovascular diseases (Cohen et al. 2017; Pope and Dockery 2006).

Atmospheric PM_{2.5} includes inorganic and organic species such as ammonium (NH_4^+), sulphate (SO_4^-), nitrate (NO_3^-), chloride (Cl^-), organic aerosol (OA), elemental carbon (EC), etc., and trace metals (Jimenez et al. 2009; Zhang et al. 2000). OA constitute a dominant fraction (~20 to 90%) of PM_{2.5} on a global scale and are directly emitted from combustion sources, such as burning wood and traffic-related (vehicular) activities, in particle phase as primary organic aerosol (POA) (Jimenez et al. 2009; Kanakidou et al. 2005; Pöschl 2005). They can also form as secondary organic aerosol (SOA) through a variety of gas-phase and multiphase heterogeneous reactions, resulting in gas-to-particle transformations (Lee Ng et al. 2017; Papapostolou et al. 2013; Hallquist et al. 2009; Jimenez et al. 2009; Kanakidou et al. 2005). The gas-phase reactions, involving oxidants (such as OH radicals, ozone (O_3), and nitrate (NO_3) radicals, etc.) and volatile organic compounds (VOCs), produce products of diverse volatility. A large fraction of these products condenses (multiphase process) onto existing particles (Ylisirniö et al. 2020; Palm et al. 2016). Products having sufficiently lower volatility than parent VOC can partition into the particle phase directly, forming SOA (Donahue et al. 2006; Pankow 1994). SOA formation can also occur through aqueous-phase oxidation in

fog and cloud droplets (Choudhary et al. 2024; Ervens 2015; Zhao et al. 2015; Ervens et al. 2011; Lim et al. 2010).

The physicochemical characteristics of POA and SOA are different (Srivastava et al. 2022; Delfino et al. 2010), and thus, there will likely be corresponding differences in toxicity. So far, most research on cellular toxicity (*in vitro*) of air pollutants has focused on those directly emitted into the atmosphere, primarily as POA. In this regard, previous studies reported that exposure to POA from sources such as wood burning (Wang et al. 2021; McCarthy et al. 2017; Longhin et al. 2016) and traffic-related activities (Rossner et al. 2021; Wang et al. 2021; Pang et al. 2020; Longhin et al. 2016) can induce oxidative stress and inflammatory responses in human lung cells, resulting in cell damage. The few recent studies (such as Chowdhury et al. 2018) that have investigated the effects of SOA exposure on cells, observed remarkably enhanced oxidative stress and inflammatory responses. Controlled human exposures, using facilities such as the Air Pollution Exposure Laboratory (APEL) (Birger et al. 2011), have also been based on air pollutants directly emitted from combustion sources (Long et al. 2022; Wu et al. 2018; Rider et al. 2016; Peretz et al. 2008; Mills et al. 2007; Nordenhäll et al. 2000). However, these exposures do not fully represent the real-world ambient air pollution composition, as ambient air exposures are influenced by atmospheric aging, which includes the formation of SOA. To the best of our knowledge, except for Schuck and Rogers 1959, no study has used aged air pollution, either from wood burning or traffic-related activities – two primary sources of particle-rich air pollution globally – during controlled human exposures (Weitekamp et al. 2020). Schuck and Rogers 1959 found that exposure to UV-irradiated automobile exhaust causes eye irritation in humans.

Major approaches to studying the SOA formation mechanisms and evolution in the chemical composition include environmental “smog” chambers and oxidative flow reactors (OFRs). Environmental chambers have been used extensively to simulate atmospheric

oxidation (Yazdani et al. 2021; Weitkamp et al. 2007; Odum et al. 1997). However, recent studies have highlighted limitations, such as loss of particles and semi-volatile compounds to chamber walls, especially with longer (> 1 day) residence times (Krechmer et al. 2015, 2016; Ye et al. 2016; Pathak et al. 2007). Besides these limitations, environmental chambers usually have large volumes (2 to 256 m³) making them unsuitable for fieldwork and only allow atmospheric aging equivalent to a maximum of a few days (Wu et al. 2007; Mentel et al. 1996). OFRs are much smaller (1 L to 1 m³) than environmental chambers (Wu et al. 2023; Xu and Collins 2021; Huang et al. 2017; Keller and Burtscher 2012; Lambe et al. 2011; Ezell et al. 2010; Kang et al. 2007) and usually employ higher oxidant concentrations, allowing hours to months of equivalent atmospheric aging in a very short residence time (seconds to minutes), with reduced wall interactions. Furthermore, the portability of OFRs ensures their applicability in both laboratory and field studies. However, OFRs can be subjected to unusual aging reactions compared to the ambient atmosphere, due to different regimes of oxidation processes (Peng and Jimenez 2020; Peng et al. 2016). OFR design parameters, such as flow profile, residence time distribution (RTD), wall losses, vapor losses, and oxidation reactions, can influence these different regimes in OFRs. Regardless of these limitations, OFRs for SOA formation are well-established, and numerous previous studies have used OFRs to simulate the formation of SOA from wood smoke (Wu et al. 2023; Wang et al. 2022; Ortega et al. 2013) and traffic-related emissions (Ihalainen et al. 2019; Simonen et al. 2017) in the laboratory. A few studies also used OFRs to investigate SOA formation in the ambient atmosphere (Xu and Collins 2021; Palm et al. 2016).

In the present study, we demonstrate the design and characterization of a new custom-built OFR called the Fast-oxidation Box (hereafter referred to as FoxBox), devised to achieve a more realistic air pollution composition for controlled human and cell exposures. FoxBox's design aimed to ensure a narrow RTD, a short residence time, limited contact of the sample

with reactor walls, and real-time measurements to track physicochemical changes in the sample. The goal of this work is to test the effectiveness and utility of the FoxBox for laboratory-based photochemical aging and highlight its potential in furthering our understanding of how atmosphere-like aging of aerosol may alter molecular signaling pathways in human lung cells.

2. Experimental

The following experiments were conducted to evaluate the performance of FoxBox: (a) RTD measurements corresponding to CO₂, SO₂ and particles present in diesel exhaust (DE), (b) particle transmission efficiency measurements, (c) fates of low-volatile organic compounds (LVOC) in the FoxBox, including losses to the reactor walls, and (d) measurements of size distribution, SOA formation, and aerosol mass spectra of DE during OH exposures. In addition, a case study was carried out to examine the viability of human lung cells after *in vitro* exposure to fresh and aged DE. All these experiments were performed with DE particles generated within our laboratory.

Fig. 1 shows a schematic of the experimental setup used in this study. The diesel engine (Euro-Stage 5 compliant, 4.5kW 1B30E Hatz engine) was used as the source of gases and particles. The engine produces an exhaust flow of 580 LPM through an engine exhaust line, most of which is vented to the outdoor atmosphere because it is in excess of what is needed for our experiments (Birger et al. 2011). A small amount of DE is diluted with HEPA filtered air and is connected to the booth directly (via a bypass flow pipe) or through the FoxBox. The amount of DE fed into the booth depends on speed of the exhaust fan controlled at the exit of the booth. A 3-way valve was placed upstream of the booth and FoxBox to switch flows. Several gas and particle measurement instruments were operated at the FoxBox exit (point A) and the booth (point B). The flow rates of DE injections into the FoxBox were controlled at the

exit of the booth by regulating the speed of the exhaust fan (point C) using a remote controller (thus, we have referred to it as exhaust flow rate in this study). More details about the experimental setup, such as FoxBox design, experiments carried out for FoxBox characterization, and instruments used, are discussed in the following sections.

2.1. Description of FoxBox

The FoxBox is a custom-built OFR at APEL, based on the principle of Potential Aerosol Mass (PAM) (Kang et al. 2007). The FoxBox was constructed using sheets of aluminum alloy, a conductive and corrosion-resistant material under real-world atmospheric conditions, including a pH range from 4 to 7 (Kutz 2012). These characteristics inhibit electrostatic losses in OFRs (Lambe et al. 2011). The reactor is 182.9 cm tall, 61.0 cm deep and 91.4 cm wide. It has a total volume of 1.019 m³ (1019 L) and a surface-area-to-volume ratio of 2 m⁻¹, much lower than other operational OFRs, e.g., Caltech (24 m⁻¹) (Huang et al. 2017), TPOT (56 m⁻¹) (George et al. 2007), and PAM (25 m⁻¹) (Lambe et al. 2011).

The FoxBox houses four pairs of UV lamps (Atlantic Ultraviolet Ster-L-Ray Germicidal Lamp), as shown in Fig. 1, with each pair equally spaced 42 cm apart and 31 cm separating the lamps in each pair. Moreover, each pair comprises one 185 and one 254 nm UV lamp. The lamps are 84 cm long and housed in 91-cm-long Teflon tubes. One pair (Pair I, Fig. 1) of lamps is wrapped in Teflon tape to decrease the intensities of 185 nm UV-light, compared to 254 nm. The 185 nm UV-lamps in the FoxBox are responsible for the production of O₃ and some OH whereas the 254 nm lamps dissociate O₃ to form an excited-state O atom, which reacts with H₂O to form most of the OH radicals. The production of O₃ and OH radicals can be controlled by regulating UV irradiation (photon flux) inside the FoxBox. To control the extent of UV irradiation, the four pairs of lamps (3 normal pairs, 1 with Teflon tape) can be activated independently. A compressed nitrogen gas tank (Praxair) is connected to the reactor, and was

used to purge the space around the UV lamps within the Teflon tubes to prevent O₃ formation around the lamps. The purging process also helps to minimize the heat generated by UV lamps, which warms the OFR walls and the air inside.

2.2. FoxBox residence time distributions

RTDs of gases and particles for the FoxBox were characterized by injecting 20s pulses of DE into the reactor. DE-derived CO₂ and SO₂, surrogates for wall-inert and wall-adhering species, respectively, were used to characterize RTDs of gases, whereas DE particles were used for the condensed-phase species. Prior to RTD measurements, the FoxBox walls were passivated with DE until steady concentrations were achieved for the above-mentioned species, at which time the DE injection into the FoxBox was stopped and the concentrations returned to near background levels. The flow rates used for RTD measurements were those needed to maintain a suitable air exchange in the booth during controlled human exposures, which is crucial for the comfort of the participant (Birger et al. 2011). It is noted that the booth at the APEL has a total volume of 4760 L (4.76 m³, 121.9 cm wide × 182.9 cm deep × 213.4 cm tall). Thus, the flow rate of air pollutants (e.g., DE) into the booth was >1300 LPM, providing an air exchange time of < 3.5 minutes within the booth. As a result, the RTDs were measured at three flow rates, 1300, 1850, and 2450 LPM in this study, to determine the optimized flow rate for photochemical aging in the FoxBox (Reynolds number (Re) > 4340, turbulent flow conditions) and their effect on the FoxBox residence time. CO₂, SO₂ and optical particle sizer (OPS)-derived total particle number concentrations were measured at the immediate FoxBox outlet (point A in Fig. 1). All experiments were repeated thrice, and the concentrations were background corrected.

Background corrected RTD measurements were used to determine RTD-weighted mean time (RTD_{mean}), an approximation of residence time, of the FoxBox using the following equation (Cao et al. 2020):

$$RTD_{\text{mean}} = \frac{1}{C_i} \times \sum_{t=2}^T (t \times C_{i,t}) \quad (1)$$

$$C_i = \sum_{t=2}^T C_{i,t} \quad (2)$$

where RTD_{mean} is the residence time of FoxBox (s), C_i is the total concentration of species i (ppbv or cm^{-3}), $C_{i,t}$ is the concentration of species i at time t (ppbv or cm^{-3}), t is the time at which C_i is measured, and T is the total time length of the pulse from injection to return to baseline.

2.3. Particle transmission efficiency

Size-dependent particle transmission efficiencies in the FoxBox were examined using polydisperse DE particles with mobility diameters of 14.6 to 615.3 nm. Transmission efficiency was calculated from measurements of particle number size distribution at the inlet and at the outlet of the FoxBox. The particle number size distribution at the inlet was measured by switching a steady DE flow directly into the booth (via bypass flow pipe, at point B in Fig. 1), whereas the measurements at the FoxBox outlet were obtained by switching the DE flow to the booth chamber via the FoxBox (point B in Fig. 1). Furthermore, the size-dependent particle transmission efficiency was calculated as the ratio of background-corrected particle number concentrations measured at the outlet (i.e., via FoxBox) and inlet (i.e., bypass) of the FoxBox. The transmission efficiency measurements were repeated thrice, each at a steady total particle number concentration ranging from 50000 to 60000 cm^{-3} . The equivalent $PM_{2.5}$ concentration ranged from 35 to 55 $\mu\text{g m}^{-3}$ (standard deviation was within $\pm 5 \mu\text{g m}^{-3}$ for each repetition).

2.4. Chamber wall index (CWI)

Controlled aging experiments in atmospheric environmental enclosures, such as environmental chambers, OFRs, etc., are susceptible to wall influence that can alter the aging chemistry. Many different sizes, shapes, and flow characteristics of enclosures are operational worldwide (Table S1 of the supplementary file); however, it is very difficult to determine which enclosure design has less wall influence on the chemistry. Chamber wall index (CWI; Brune 2019) is a simple metric which represents the degree to which the chemistry in an enclosure is free from unwanted wall effects (e.g., uptake, surface chemistry, etc.) as governed by sampled gas-phase chemical constituents related to SOA formation. In this study, CWI was determined using the following equation (Brune 2019):

$$CWI = \frac{V}{A} \times \frac{1}{\tau_{RTD_mean}} \times \left(\frac{\arctan\left(\delta_c \times \sqrt{\frac{k_e}{D_g}}\right)}{\sqrt{k_e \times D_g}} + \frac{4}{a_w \times \omega} \right) \quad (3)$$

where V is the volume of the enclosure (m^3), A is the surface area (m^2), τ_{RTD_mean} is the weighted-mean residence time (s), D_g is the gas-phase diffusion coefficient of the species ($m^2 s^{-1}$), k_e is the eddy diffusion frequency (s^{-1}), δ_c is the chemical boundary layer depth (m), a_w is the accommodation coefficient for the chemical species on the wall, and ω is the molecular speed of the chemical species. We have determined the CWI for the FoxBox in this study and compared it with several other widely used environmental chambers and OFRs worldwide. The detailed information on V , A , τ_{RTD_mean} and δ_c of these enclosures is shown in Table S1. D_g , a_w and ω values of $5 \times 10^{-6} m^2 s^{-1}$, 1 and $180 m s^{-1}$ were adopted from previous studies (Brune 2019). The k_e was calculated using the following equation (Brune 2019; Krechmer et al. 2016; Palm et al. 2016):

$$k_e = 0.004 + 10^{-2.25} \times V^{0.74} \quad (4)$$

2.5. OH exposure levels

OH exposure (OH_{exp}), indicating OH radical concentration integrated over time, is a key parameter for interpreting photochemical aging in an OFR. Several previous studies (Wu et al. 2023; Lambe et al. 2011, 2015; Li et al. 2015) have used the decay of SO_2 during photochemical oxidation in the OFR to determine the OH_{exp} levels. In this study, a steady DE flow was introduced into the FoxBox under distinct UV-light exposures and the decay in SO_2 (present in DE) was monitored at the FoxBox exit (point A as shown in Fig. 1) to quantify OH_{exp} levels. In total, five different combinations of UV-lamps (Pair I, Pair II, Pairs I+II, Pairs I+II+III, and Pairs I+II+III+IV lamps) produced distinct UV-light exposures. The measurements were conducted in triplicates for each UV-light exposure. The following equation was used to calculate OH_{exp} :

$$\text{OH}_{\text{exp}} = \frac{1}{k_{\text{OH-}\text{SO}_2}} \ln \left(\frac{[\text{SO}_2]_0}{[\text{SO}_2]_f} \right) \quad (5)$$

where $k_{\text{OH-}\text{SO}_2}$ is the reaction rate constant of SO_2 with OH, and $[\text{SO}_2]_0$ and $[\text{SO}_2]_f$ are the concentrations of SO_2 before and after photochemical oxidation in the FoxBox, respectively. The $k_{\text{OH-}\text{SO}_2}$ of $9.2 \times 10^{-13} \text{ cm}^3 \text{ molec}^{-1} \text{ s}^{-1}$ was used in equation 5 in this study (Peng et al. 2015; Sander et al. 2011). Furthermore, OH_{exp} was normalized to the daily average OH concentration to calculate the photochemical age of aged aerosol. We used a daily average OH concentration of $1.5 \times 10^6 \text{ molec cm}^{-3}$ to convert the OH_{exp} to atmospheric equivalent photochemical age (Mao et al. 2009).

These photochemical oxidation measurements at different UV-light exposures were based on a steady DE flow, equivalent to $\text{PM}_{2.5}$ concentration varying from 280 to $350 \mu\text{g m}^{-3}$. The O_3 , $\text{PM}_{2.5}$, organic carbon (OC), EC, particle number size distribution, and aerosol mass spectra measured along with SO_2 monitoring during the photochemical oxidation. More details on these measurements are discussed in section 2.7.

2.6. Low-volatile organic compound (LVOC) fates

SOA formation as a function of age in OFRs depends on the timescales of distinct competing processes and their relative importance compared to the atmosphere. During photochemical oxidation in OFRs, organic vapors (also referred to as VOCs) are oxidized, forming low-volatility VOCs (LVOCs). These LVOC compounds effectively condense onto existing particles irreversibly. In the atmosphere, the dominant fate (loss) of LVOCs is condensation onto particles (atmospheric lifetime of \sim minutes) (Knote et al. 2015; Nguyen et al. 2015). However, due to different timescales and experimental conditions in OFRs (e.g., short residence times of \sim seconds to minutes, high oxidant concentrations, etc.), the LVOCs formed can have other fates besides condensation onto aerosol (Palm et al. 2016). These other fates include condensational losses to the surface of OFR walls, further reaction with OH radicals to produce highly volatile gas-phase products (e.g., CO_2), and exiting the OFR in the gas phase (in that case LVOCs will entirely condense on the sampling tube walls due to the large surface-area-to-volume ratio). The OFR measurements must be corrected for these other fates to closely relate SOA formation processes in OFRs, with real atmospheric processes.

In this regard, (Palm et al. 2016) discussed a method to estimate LVOC fates in OFRs, including condensation onto particles, condensation on the surface of reactor walls, reaction with OH, and the fraction of LVOC exiting the OFR. In this study, we examined LVOC fates corresponding to high condensation sink (CS) and low CS scenarios. The high CS scenario ($> 3.5 \times 10^5 \text{ s}^{-1}$) was based on photochemical oxidation of DE at $\text{PM}_{2.5}$ concentrations of 280 to $350 \mu\text{g m}^{-3}$, whereas low CS ($< 2.0 \times 10^5 \text{ s}^{-1}$) was based on photochemical oxidation of DE at $\text{PM}_{2.5}$ of 80 to $100 \mu\text{g m}^{-3}$. A detailed description of the method used to estimate LVOC fates for the FoxBox is given in section S1 of the supplementary file. We also used same method to estimate LVOC losses for the FoxBox in the absence of CS and oxidants, to determine the upper limit of LVOC wall losses.

2.7. Gas and particle generation and their monitoring

The production of DE followed a standardized process developed in the APEL (Birger et al. 2011) to simulate on-road highway conditions. This process includes loading the engine from idle up to 4kW with increments of 0.5kW at ~5 min intervals, followed by a simulated cruising condition at 3kW where the engine remains for the duration of the experiment. A small amount of DE was drawn from the engine tailpipe, diluted, and fed into the booth either directly or via the FoxBox, as shown in Fig. 1. The exhaust flow rates of DE injections were measured by a flowmeter (Dwyer, VFC-121) at point C (Fig. 1).

A multitude of instruments were placed at the exit of the FoxBox (point A) and booth (point B) to monitor the gases and aerosol in DE (Fig. 1). For monitoring gases, CO₂ (Thermo Scientific™ Model 410i), CO (Thermo Scientific™ Model 48i-TLE), SO₂ (Thermo Scientific™ Model 43i), NO_x (Thermo Scientific™ Model 42i-LS), and O₃ (Thermo Scientific™ Model 49i) analyzers were used to measure the CO₂, CO, SO₂, NO/NO₂/NO_x and O₃ concentrations, respectively. A tapered element oscillating microbalance (TEOM) (Rupprecht & Patashnick Co. Series 1400a) was used to measure PM_{2.5} mass concentrations. An OPS (TSI Model 3330) was used to measure total particle number concentration from 0.3 to 10 µm diameter. All the above-mentioned parameters were measured at two-second intervals. Furthermore, a Graywolf TG-503 probe, set up within the booth, measured the total VOC (TVOC) concentrations, temperature and relative humidity (RH, %) at one-minute intervals. A humidifier (Nortec) maintained sufficient RH (approximately 40%) inside the FoxBox and booth. A scanning mobility particle sizer (SMPS; TSI Model 3936) measured the number and mass size distribution of aerosol particles from a mobility diameter of 14.6 to 615.3 nm at a sample flow rate of 0.3 LPM and a sheath flow rate of 3 LPM. The SMPS consists of two units: an electrostatic classifier (TSI Series 3080) and a condensation particle counter (TSI Model 3775). The data from the SMPS were recorded at 3-minute intervals.

A High Resolution Time-of-Flight Aerosol Mass Spectrometer (HR-ToF AMS; Aerodyne) operating in V-mode (DeCarlo et al. 2006; Jimenez et al. 2003) measured the aerosol mass spectra to look for signs of aerosol aging and SOA formation. Data analysis was performed using SQUIRREL 1.66G and PIKA 1.26G. Elemental ratios (O:C and H:C) were determined with the improved ambient method (Canagaratna et al. 2015). A few other well-established AMS parameters that were explored included f_{43} (the fraction of carbon with m/z 43) (Ng et al. 2010), f_{44} (the fraction of carbon with m/z 44) (Ng et al. 2010), and f_{57} (the fraction of carbon with m/z 57). These parameters retrieved from the unit mass data, and represents all the fragments at m/z 43 (mainly $C_3H_7^+$ and $C_2H_3O^+$), m/z 44 (mainly CO_2^+) and m/z 57 (mainly $C_4H_9^+$ and $C_3H_5O^+$), respectively. All these data were recorded in real-time during the experiment so that the operator could effectively control the system. Additionally, eighteen particle-laden quartz filters (Blanks = 3, fresh DE = 3, aged DE = 12) were collected at the exit of the booth at 10 LPM flow rate using a Harvard impactor, for offline measurements of EC/OC. EC/OC were measured using the National Institute of Occupational Safety and Health (NIOSH) 5040 protocol based on thermal optical transmittance on a total carbon analyzer (Sunset Laboratory Inc.).

2.7. *In vitro* cell exposure and cell viability measurements

In this study, we used the human alveolar epithelial cell line A549 for *in vitro* exposures. A detailed description of culture conditions and the exposure system is given in section S2 of supplementary file. Briefly, cultured A549 cells (initial seeding concentration of 5×10^4 cells/mL), at in lab passages 5-20, were subjected to fresh or aged DE exposures equivalent to $\sim 350 \mu g m^{-3}$ $PM_{2.5}$ concentration for 1 h using the CULTEX[®] RFS exposure system (Aufderheide et al. 2013; Aufderheide 2005). In parallel, identical cells were exposed to lab air passed through HEPA activated carbon filters (FA). One set of these cells were left within the incubator (INC) as an additional control. All three sets were collected for each DE exposure.

We repeated each cell exposure (fresh DE and aged DE) twice in triplicate inserts (total six inserts collected). After each exposure, cell inserts were stored in the incubator at 37°C with 5% CO₂ for 24 hours.

After 24 h, DE (fresh and aged) exposed cells and their respective FA and INC controls were analyzed for cell viability using MTT (3-(4, 5-dimethylthiazolyl-2)-2, 5-diphenyl tetrazolium bromide) assays, according to the manufacturer's instructions (Sigma Aldrich). This method is based on the dissolution of MTT to formazan in the presence of viable cells or active cellular metabolic activity (Hansen et al. 1989). For MTT assay measurements, firstly, we prepared the reagent mixture (consisting of thiazolyl blue tetrazolium bromide) at a 1 mg/mL concentration in Hank's Balanced Salt Solution (HBSS) with calcium chloride and magnesium chloride (Gibco™, Thermo Fischer Scientific). The apical media was aspirated, and the cells were washed one time using 100 µL same HBSS solution. Subsequently, 50 µL of MTT reagent solution was added to each Transwell (apical), and the cells were incubated at 37°C with 5% CO₂ for 30 min. After 30 min, the MTT reagent solution was aspirated from the Transwells. Subsequently, 55 µL of DMSO was added to each well for cell lysis, after which the Transwells were placed on a shaker until a homogeneous solution was formed. Thereafter, 50 µL of DMSO/cell lysate mixture from each well was transferred onto a 96-well plate, along with a couple of DMSO-only blanks. The absorbance at 584 nm was measured using a plate reader (SpectraMax i3x). These absorbance measurements were then used to calculate % cell viability using the formula:

$$\% \text{ cell viability} = \frac{A_{\text{sample}}}{A_{\text{INC}}} \times 100 \quad (6)$$

where A_{sample} indicates absorbance at 584 nm (corrected for blank, DMSO only, absorbance) for fresh DE, aged DE, and FA exposed cells, and A_{INC} is blank corrected absorbance for incubator controls.

3. Results and discussion

3.1. Residence time distributions (RTDs) of the FoxBox

The RTDs of the FoxBox were experimentally characterized with a wall-inert gas (CO_2), a wall-adhering gas (SO_2), and physiochemically heterogeneous (atmospherically relevant) DE particles, with UV lamps turned off. Figs. 2a and 2b show representative RTDs measured for CO_2 (produced from the engine) and particles with pulsed input (20s) into the FoxBox, respectively. Fig. S1 in the supplementary file shows RTDs measured with SO_2 . The same pulse (of DE) introduced to the FoxBox, as discussed in section 2.2, was used to obtain RTDs for all these species.

The first result is that the shape and width of the RTDs are all invariant as a function of flow rates from 1300 to 2450 LPM for CO_2 (Fig. 2a), SO_2 (Fig. S1), and particles (Fig. 2b). RTD_{mean} , an approximation of the average residence time of the FoxBox, also reflects these observations (Table S2). The RTD_{mean} values were 59s, 58s, and 59s measured with CO_2 , 195s, 187s, and 190s measured with SO_2 , and 30s, 30s, and 28s measured with particles at 1300, 1850, and 2450 LPM flow rates, respectively (Table S2). The residence times being the same at the different flow rates may look surprising, as ideally, with the increase in the flow rate, the air must have moved through the FoxBox faster, reducing the residence time of an individual molecule/species by the inverse of the mass flow rate. However, as discussed above, the amount of DE fed into the booth (and FoxBox) depends on the speed of the exhaust fan controlled at the exit of the booth (point C shown in Fig. 1). We fed a 20s pulse of the DE to the FoxBox. While the pulse length in time was the same, for a slower flow rate, the pulse length was shorter in terms of the amount of DE (or length along the tube (pipe) occupied by DE) to which the flow was added. For higher flow rates, the amount of DE added to the flow was much greater (a longer length along the tube/pipe occupied by DE). As a result, the amount of time taken to

clear the FoxBox is the same for all flow rates. The fact that the residence times were the same for all flow rates in this study, and that the actual residence time for a molecule depends linearly on the inverse of the flow rate, suggests that the flow pattern (turbulent flow) inside the FoxBox does not change substantially at the different flow rates.

The second result is that the RTDs for particles (Fig. 2b) were narrowest, followed by CO₂ (Fig. 2a) and SO₂ (Fig. S1) in that order, demonstrating that the particles passed through the FoxBox more quickly than CO₂, with SO₂ being the slowest. The average residence time estimates for particles, CO₂, and SO₂, were 30s, 58s, and 190s, respectively (Table S2), consistent with these observations. This difference is plausibly due to either (a) comparatively poorer mixing of particles into the carrier gas (HEPA filtered air) flow than CO₂ and SO₂ before entry into the FoxBox or (b) greater losses of particles to the FoxBox walls (discussed in section 3.2) due to entrainment in eddy currents. Furthermore, RTDs for SO₂ were delayed relative to CO₂, as discussed above. The delay indicates enhanced interactions of SO₂ with the FoxBox walls, due to its sticky nature in comparison to CO₂. Without wall interactions, RTDs for both SO₂ and CO₂ would be expected to be the same. These observations highlight wall effects, especially on gas-phase precursors, in the FoxBox.

Figs. 3a and 3b show probability distribution functions of residence time for gases (i.e., CO₂) and particles, respectively. Reporting the RTD measurements as normalized distribution functions enables the comparison of one OFR's flow characteristics with others with different shapes and sizes. RTDs of an idealized device (laminar flow) (Huang et al. 2017) and those observed or reported for the FoxBox (this study), PAM (Lambe et al. 2011), and CPOT (Huang et al. 2017) are shown in Figs. 3a and 3b for comparison (PAM Wiki). The residence time probability distribution function is defined as the normalized measured concentration ($C_{\text{out}}(t)$) divided by the total area of the normalized pulse (Simonen et al. 2017; Fogler and Gürmen 1999), as given below:

$$\text{PDF}(t) = \frac{C_{\text{out}}(t)}{\int_0^{\infty} C_{\text{out}}(t) dt} \quad (7)$$

where t is the residence time normalized to the average residence time (RTD_{mean}) of the OFR. We observed the residence time probability distribution function of CO_2 and particles in the FoxBox OFR, as shown in Figs. 3a and 3b, respectively, resembled those expected for ideal laminar flow. Yet, the pulses were slightly broader for CO_2 compared to laminar flow. Additionally, both pulses (CO_2 and particles) for the FoxBox were similar to PAM and CPOT (Fig. 3). Previous studies reported that the heat generated by UV lamps can warm up the OFR walls and enhance convection inside the OFR, which may broaden the RTD (Simonen et al. 2017). However, we did not observe any such effect on RTDs of both CO_2 and particles under UV exposure, compared to when UV turned off (Fig. 3), indicating that the heat generated by UV lamps had either no, or minimal, effects on the RTDs. Circulation of N_2 gas through the housing around the UV lamps is likely to have minimized convective mixing in the FoxBox by quickly replacing air surrounding the UV lamps.

3.2. Transmission efficiency of particles

As stated above, particle transmission efficiency is defined as the ratio of the particle number concentration exiting the reactor to that exiting the bypass flow pipe. The particle number size distributions of DE exiting the FoxBox and bypass flow pipe are shown in Fig. S2. Fig. 4 shows the transmission efficiency of DE particles as a function of mobility diameters ranging from 15 to 615 nm. We observed that the particle transmission efficiency was slightly lower for smaller sized particles, ~95% for particles < 40 nm (i.e., ~5% loss of < 40 nm particles). Moreover, particles with a mobility diameter > 40 nm could transmit through the FoxBox with ~100% efficiency. These observations indicate that particle losses in the FoxBox are negligible. Thus, no correction of particle losses to the walls is required during photochemical aging (of DE, wood smoke, etc.) studies in the FoxBox.

We compared the particle transmission efficiency of FoxBox with other OFRs, such as CPOT (Huang et al. 2017), TPOT (Lambe et al. 2011), and PAM (Lambe et al. 2011) (Fig. 4). Monodisperse ammonium sulfate (AS) particles were used to determine particle transmission efficiency of CPOT, whereas bis(2-ethylhexyl) sebacate (BES) particles were used for the TPOT and PAM reactors. As shown in Fig. 4, significant particle losses were reported for these reactors, compared to the FoxBox. For example, both the PAM (Lambe et al. 2011) and CPOT (Huang et al. 2017) reactors have been reported to undergo significant particle losses not only for smaller mobility diameters but also for large particles (~20%) with diameters > 100 nm. For the TPOT reactor, the particle losses at smaller mobility diameters were highest among all the reactors, whereas losses were similar to CPOT and PAM at larger diameters. The critical factor behind the almost negligible particle losses found in the FoxBox is the very high flow rate used (lower residence time = ~30s) for measurements compared to the other reactors (~100 to 600s). Another key factor could be that the FoxBox is made of aluminum alloy sheet, whereas all the reactors mentioned above are made of glass. In this context, a previous study (Lambe et al. 2011) has reported that conductive materials (e.g., aluminum) are less prone to particle losses than glass and all more recent PAM reactors are now coated with aluminum (Aerodyne 2019).

3.3. Fate of low-volatile organic gases in FoxBox

Earth's oxidizing atmosphere dictates the fate of thousands of chemically distinct air pollutants emitted into the atmosphere via several aging processes (e.g., heterogenous OH oxidation, photolysis, etc.) involving the production of oxidative reactants such as O₃, OH radicals, etc., and SOA. As discussed above, OFRs can simulate the chemical processes occurring in the atmosphere; however, OFRs are susceptible to wall influences that can alter the chemistry of these processes. The CWI metric (Brune 2019) indicates the degree to which the OFR is free from potential unwanted wall losses of gas-phase air pollutants, especially

organics which are associated with SOA formation. Overall, the mean CWI values for OFRs were higher than those for environmental chambers, indicating that walls alter the chemistry less in OFRs than in environmental chambers (Fig. S3). Furthermore, we found that the CWI of FoxBox, estimated at ~50, was very high in comparison to all the other OFRs (varying from ~0.5 to 2.5) and environmental chambers (varying from 0.1 to 0.2). These observations signify that wall losses of gas-phase air pollutants (e.g., semi- and low-volatile VOCs) in the FoxBox are negligible compared to the existing OFRs and environmental chambers, due primarily to its lower residence time (~58s) in comparison to the other reactors (~100 to 600s) and environmental chambers (hours).

The dominant fate of LVOCs in the atmosphere is condensation onto aerosol particles (Palm et al. 2016; Knote et al. 2015; Nguyen et al. 2015). However, LVOC fates in the OFR include condensational losses to the OFR walls, losses due to reaction with OH to produce highly volatile gas-phase products, and a fraction exiting the OFR in the gas phase (completely lost to sampling tube walls) along with condensation onto aerosol (Palm et al. 2016). We estimate the upper limit of LVOC losses to the FoxBox walls in the absence of CS and oxidants to be around 6%. The FoxBox LVOC losses were significantly lower than those of other OFRs. The estimated upper limit of LVOC losses was around 20% for the RAAD OFR (Wu et al. 2023), and approximately 30% for the PFA OFR (Xu and Collins 2021). These findings indicate that the FoxBox is a highly efficient reactor, with negligible susceptibility to gas and particle losses.

3.4. Photochemical oxidation of DE in the FoxBox: Evolution of physicochemical characteristics

Photochemical oxidation of DE in the FoxBox was carried out under five different UV exposure conditions, as discussed in section 2.5. The oxidation process is known to be

influenced by RH conditions in the reactor. Therefore, we maintained nearly consistent RH and temperature levels of $(40 \pm 5)\%$ and $(24 \pm 1)^\circ\text{C}$, respectively, during the oxidation. The equivalent water mixing ratio at 1.3%, estimated using RH values in OFR_Exposures_Estimator_v3.1 (PAM Wiki), was greater than the 0.8% prescribed for safer (atmospherically relevant) photochemical oxidation (Peng and Jimenez 2020; Peng et al. 2015, 2016). The maximum OH_{exp} achieved was approximately 1×10^{12} molecules per cubic centimeter second ($\text{molec cm}^{-3} \text{ s}$), equivalent to approximately 8 days of atmospheric aging. It varied from about $0.2 \times 10^{12} \text{ molec cm}^{-3} \text{ s}$ for no output O_3 to $1 \times 10^{12} \text{ molec cm}^{-3} \text{ s}$ for 600 ppbv of output ozone (Fig. S4). As 8 days of equivalent photochemical age generally meets the requirements of most aging experiments, we did not measure the maximum OH_{exp} that can be produced in the FoxBox.

As discussed earlier, the OH_{exp} calculations in this study were based on SO_2 decay measurements. The OH_{exp} determined by SO_2 decay may or may not be a good indicator of true OH_{exp} . In this context, previous studies (Peng and Jimenez 2020; Richards-Henderson et al. 2016; Kan et al. 1981) have reported that peroxy radicals (RO_2), primarily form as a result of a reaction between OH and VOCs in OFRs, can react with SO_2 . The reaction rate of $\text{RO}_2 + \text{SO}_2$ depends quadratically on RO_2 concentration (Richards-Henderson et al. 2016; Kan et al. 1981). However, the production of RO_2 in OFR is limited by the OH oxidation of VOCs (Peng and Jimenez 2020). In simple words, the $\text{RO}_2 + \text{SO}_2$ reaction would significantly contribute to SO_2 decay only if the OH reactivity of all VOCs (OHR_{VOC}) is very high in OFRs (in the order of hundreds of s^{-1}) (Peng and Jimenez 2020). In this study, the OHR_{VOC} varied from 27 to 61 (43 ± 17) s^{-1} (Table S3), indicating a very limited or negligible role of RO_2 in SO_2 decay. Thus, SO_2 decay observed during photochemical oxidations in FoxBox is likely due to OH radicals only, signifying the reliability of OH_{exp} calculations in this study.

In addition, we have estimated the fates of LVOC in the FoxBox based on the given OH_{exp} values under both high and low CS conditions (Fig. S5). We found that at least 99.8% of LVOCs in the FoxBox were lost due to condensation onto exiting aerosol particles, similar to the actual atmosphere. The contribution of other fates to LVOC losses was less than 0.2%. All these observations demonstrate the high suitability of the FoxBox for laboratory-based photochemical oxidation of air pollutants. The impact of photochemical oxidation of DE in the FoxBox on its physicochemical characteristics (e.g., particle size distribution, SOA formation, aerosol mass spectra, etc.) is examined in the following section.

3.4.1. Particle size distribution

Fig. 5 depicts the changes in the SMPS based particle number size distribution of DE photochemically oxidized in the FoxBox over a range of OH_{exp} levels, from 3.0×10^{11} to 9.5×10^{11} molec cm^{-3} s (equivalent photochemical ages: 2.3 to 7.6 days), compared to fresh DE. An initial observation of fresh DE revealed a unimodal particle size distribution with a median size of 119 nm. Distinct bimodal size distributions were observed at different OH_{exp} levels for aged DE. In fact, the median size of the particulate emissions decreased as OH_{exp} levels increased, dropping from 119 nm for fresh DE to 48 nm for aged DE at an OH_{exp} of 9.5×10^{11} molec cm^{-3} s. This decrease was due to substantial new ultrafine particle formation and their growth in nucleation mode (from 20 to 50 nm) with increased OH_{exp} levels during photochemical oxidation. In simpler terms, higher OH_{exp} levels led to an increase in ultrafine particle concentrations in nucleation mode. Based on previous studies (Akherati et al. 2020), we believe that the observed nucleation likely resulted from aromatic compounds present in DE being oxidized under OH_{exp} and rapidly forming SOA.

Additionally, from Fig. 5, we observed that the size of the ultrafine particles (nucleation mode) largely increased with higher OH_{exp} levels. For instance, the particle diameter in the

nucleation mode was approximately 25 nm at an OH_{exp} of 3.0×10^{11} molec cm^{-3} s, and increased to about 40 nm at 9.5×10^{11} molec cm^{-3} s. The particle diameter in the accumulation mode increased until an OH_{exp} of 3.0×10^{11} molec cm^{-3} s and slightly decreased afterwards. However, we did not observe nucleation mode in particle mass size distribution, and the mass concentration and diameter in accumulation mode largely increased with higher OH_{exp} (Fig. S6). These observations suggest that most of the oxidized VOCs (semi- and low-volatility) likely condensed onto particles in accumulation mode. In nucleation mode, either less-oxidized (semi-volatility) VOCs or, a small fraction of low-volatility VOCs or, a combination of both may have condensed onto the newly formed particles, resulting in a negligible addition to the mass concentration compared to accumulation mode. These findings are consistent with the LVOC fate model discussed above, where VOCs rapidly oxidize to semi- or low-volatility VOCs (at all OH_{exp} levels used in this study) that can condense. Furthermore, the nucleation observed during photochemical oxidation in FoxBox may not necessarily be representative of the atmosphere. In this context, previous studies have reported that a higher concentration of condensable species and oxidants in OFRs favors increased nucleation (Guo et al. 2020; Bruns et al. 2015). Thus, nucleation mode particles are a common sight in OFR-based studies (Wu et al. 2023; Zhao et al. 2021; Ihalainen et al. 2019; Simonen et al. 2017; Palm et al. 2016).

3.4.2. Evolution of aerosol mass spectra as a result of SOA formation

To investigate the formation of SOA during photochemical oxidation, the change in $\text{PM}_{2.5}$ and OC mass concentrations (also referred to as $\text{PM}_{2.5\text{ER}}$ and OC_{ER} , respectively) as a result of OH_{exp} was examined along with AMS measurements. The $\text{PM}_{2.5}$ and OC data were then used in the following equation to demonstrate SOA formation:

$$\text{OC}_{\text{ER}} = \frac{(\text{OC}/\text{EC})_{\text{OH}_{\text{exp}}}}{(\text{OC}/\text{EC})_{\text{fresh}}} \quad (8)$$

where OC_{ER} is the mass enhancement ratio of OC, $(OC/EC)_{OH_{exp}}$ is the background corrected OC/EC ratio at a given OH_{exp} , and $(OC/EC)_{fresh}$ is the background corrected OC/EC ratio for fresh (unaged) emissions. $PM_{2.5ER}$, the mass enhancement ratio of $PM_{2.5}$, was calculated by using background corrected $PM_{2.5}$ mass concentration in equation 8 instead of OC/EC ratio. Fig. 6 illustrates the changes in $PM_{2.5}$ and OC concentrations at different photochemical ages (Fig. 6a) and OH_{exp} levels (Fig. 6b), relative to fresh DE. We observed that the concentrations of both OC and OA increased with photochemical age and OH_{exp} (Fig. 6 and Fig. S7, respectively), indicating formation of SOA during photochemical oxidation in FoxBox. OC_{ER} increased from 1.3 ± 0.1 at an OH_{exp} of $(1.9 \pm 0.2) \times 10^{11}$ molec cm^{-3} s to 1.6 ± 0.1 at an OH_{exp} of $(7.0 \pm 0.5) \times 10^{11}$ molec cm^{-3} s (corresponds to photochemical age of 1.5 and 5.4 days, respectively) (Fig. 6).

The OA concentration-based mass enhancement ratio was higher, increased from ~ 1.5 at an OH_{exp} of 1.9×10^{11} molec cm^{-3} s to ~ 3.5 at an OH_{exp} of approximately 7×10^{11} molec cm^{-3} s, than OC_{ER} (Fig. S7). This difference between the ratios was likely due to comparatively higher enhancement in organic mass (OM) than OC during OH exposure (Hayes et al. 2013). Furthermore, the mass concentrations of NH_4^+ , SO_4^{2-} , and NO_3^- also increased with OH_{exp} (Fig. S7a-b). The highest increment was observed in NO_3^- concentration (9 to 26 times) followed by NH_4^+ (3 to 16 times) and SO_4^{2-} (1 to 2 times) (Fig. S7c). Despite a wide variability in mass enhancement ratios of different constituents of $PM_{2.5}$ as discussed above, the overall $PM_{2.5ER}$ was similar to OC_{ER} (Fig. 6), probably because a dominant fraction (~ 60 to 70%) of $PM_{2.5}$ in fresh DE is refractory in nature and non-refractory fraction is predominantly OA (Fig. S7a). These observations ascertain that the photochemical oxidation process leads to the secondary formation of aerosol, particularly SOA. Previous studies have also reported comparable mass enhancement ratios (~ 1.3 and 1.5) for biomass-burning derived organic aerosol after

approximately 3 and 5 days of photochemical aging in the RAAD (Wu et al. 2023), and the PAM (Ortega et al. 2013) OFR, respectively.

To investigate the chemical transformations of DE resulting from SOA formation during photochemical oxidation, aerosol mass spectra were monitored using an AMS. While the mass spectrum of fresh DE comprised almost all ions (C_xH_x) that are characteristics of hydrocarbons (e.g., $C_3H_7^+$, $C_4H_9^+$, etc.) (Fig. S8a), substantial changes (such as enhanced signal for ion types that are characteristics of oxidation (C_xH_xO , $C_xH_xO_2^+$)) were observed (e.g., $C_2H_3O^+$, CO_2^+ , etc.) in the mass spectrum of aged DE (Fig. S8b).

To further evaluate chemical transformation during photochemical oxidation, we examined fraction of certain well-established AMS-derived organic fragment (ion type) signals (m/z) to the total OA mass ($f_{m/z}$). f_{43} ($C_3H_7^+$) and f_{57} ($C_4H_9^+$) are commonly employed as proxies for freshly emitted hydrocarbon-like OA (Rajeev et al. 2022; Cubison et al. 2011; Ng et al. 2011). In addition, f_{43} ($C_2H_3O^+$) is also commonly used as a proxy for fresh SOA or less oxidized OA (Rajeev et al. 2022; Cubison et al. 2011; Ng et al. 2011). On the other hand, f_{44} (CO_2^+) represents greater oxidation (Rajeev et al. 2022; Cubison et al. 2011; Ng et al. 2011). In Fig. 7, f_{44} is plotted against f_{43} (Fig. 7a) and f_{57} (Fig. 7b) as a function of OH_{exp} levels. We found an increase in f_{44} and a decrease in f_{43} and f_{57} consistently with higher OH_{exp} levels. The f_{44} for fresh DE varied from 0.01 to 0.02 and f_{43} varied from 0.10 to 0.12. Upon photochemical oxidation, the f_{44} values consistently increased, and f_{43} decreased with higher OH_{exp} levels (~ 0.04 and ~ 0.07 , respectively, at $OH_{exp} = 9.5 \times 10^{11}$ molec cm^{-3} s) (Fig. 7a). Furthermore, f_{57} fraction decreased from ~ 0.11 for fresh DE to ~ 0.03 for aged DE (Fig. 7b).

A few previous studies (Ihalainen et al. 2019; Presto et al. 2014) have looked at photochemical oxidation of DE in an OFR and an environmental chamber. In OFR, f_{44} increased from 0.08 to 0.15, whereas f_{43} remain unchanged at ~ 0.07 at OH_{exp} of 8×10^{11} molec

cm⁻³ s (Ihalainen et al. 2019). In the environmental chamber, the f_{44} increased from 0.04 to 0.15 and the f_{43} values decreased from ~ 0.08 to 0.04 at OH_{exp} of 5.4×10^{10} molec cm⁻³ s (Presto et al. 2014). Summarily, the values of f_{43} and f_{44} observed in this study may look different from previous studies as discussed above, but, overall, the f_{43} and f_{44} values observed (or reported) in this study for fresh DE were similar to ambient hydrocarbon-like OA (f_{43} : 0.06 to 0.12; f_{44} : 0.01 to 0.04), whereas the values for aged DE were similar to ambient semi-volatile oxygenated OA (f_{43} : 0.06 to 0.15; f_{44} : 0.02 to 0.14) (Ng et al. 2011). We also examined evolution in elemental ratios of DE particles to follow oxygenation as a function of OH_{exp} levels in FoxBox, as shown in the Van Krevelen diagram (H:C versus O:C) in Fig. S9 of the supplementary file. The O:C ratio for fresh DE was ~ 0.07 and increased to ~ 0.19 for OH_{exp} of 1.9×10^{11} molec cm⁻³ s and ~ 0.23 for OH_{exp} of $(7.4 \text{ to } 9.5) \times 10^{11}$ molec cm⁻³ s. These O:C values for photochemically aged DE from FoxBox were similar to ambient semi volatility oxygenated OA (varied from 0.1 to 0.6) (Ng et al. 2011); however, they were lower than O:C values reported for low volatility oxygenated OA (varied from 0.4 to 1.0) from OH_{exp} of $(3 \text{ to } 10) \times 10^{11}$ molec cm⁻³ s by previous ambient (Ng et al. 2011) and DE-based OFR (Lambe et al. 2012) studies.

This difference is likely due to the high mass loadings (280 to 350 $\mu\text{g m}^{-3}$ fresh DE) used during photochemical oxidation in FoxBox, and as a result, even high volatility (low O/C) species could condense. Most species (VOCs) condensing were likely semi volatility rather than low volatility, resulting in the lower O:C values during OH_{exp} of DE in FoxBox. Moreover, the Van Krevelen slope for photochemical oxidation of DE in FoxBox varied from -1.6 to -1.8 and was comparable to Van Krevelen slopes reported in ambient atmosphere (including urban atmosphere enriched with vehicular pollution) (-0.8 to -1.1) (Roig Rodelas et al. 2019; Hayes et al. 2013; Heald et al. 2010). These observations and the consistency of the trend of changes in f_{43} and f_{44} during photochemical oxidation in FoxBox with other OFRs, environmental chambers, and ambient data (discussed above) indicate the atmospheric relevance of the

observations. Overall, this study of DE indicates that the FoxBox can simulate atmospherically relevant photochemical oxidation comparable to other OFRs and environmental chambers.

3.5. Cell viability of freshly emitted versus photochemically aged DE

In vitro cell exposure studies are helpful in anticipation of the integration of the FoxBox into human exposure studies. Preliminary findings from such exposures are discussed herein, focusing on cell viability, with additional details of effects at lower mass concentrations forthcoming in future publications. Thus, these cellular studies are preliminary to the suite of tests necessary before human studies can proceed. Cell viability measures the proportion of live and healthy cells within a population. A549 cells were exposed to freshly emitted and photochemically aged DE at an OH_{exp} of $7.4 \times 10^{11} \text{ molec cm}^{-3} \text{ s}$ (atmospheric equivalent photochemical age: 5.7 ± 0.4 days) in this study. Fig. 8 shows the % cell viability (relative to INC controls) after exposure to FA, fresh DE, and photochemically aged DE. The cell viability for FA (HEPA and activated carbon filtered room air) at ~97% was very similar to INC, as envisaged. The cell viability for fresh diesel exhaust was only slightly lower at 93%; however, for photochemically aged DE was much lower at 29% (Fig. 8).

A nonparametric t-test (unpaired) was used to statistically compare the cell viability of FA, fresh DE, and photochemically aged DE with INC controls. The difference in cell viability after photochemically aged DE exposures was significant ($p < 0.0001$), whereas no significant difference was identified for fresh DE. This is intriguing considering that the $\text{PM}_{2.5}$ concentrations were very similar during fresh ($339 \pm 18 \mu\text{g m}^{-3}$) and photochemically aged DE ($357 \pm 10 \mu\text{g m}^{-3}$) exposures. $\text{PM}_{2.5}$ is well known to be a major contributor to air pollution-associated adverse health effects. In this context, a recent study (Chowdhury et al. 2018) also reported that the cell viability of A549 cells decreases upon exposure to aged naphthalene- and α -pinene-derived SOA compared to fresh naphthalene and α -pinene SOA. Similar findings

have been obtained for toluene SOA as well (Yu et al. 2017). Thus, the chemical changes within PM_{2.5}, notably the formation of SOA (ultrafine particles) due to photochemical aging, are likely responsible for decreased cell viability.

However, photochemical aging also changed the fresh gaseous composition, suggesting that photochemically produced gases could also decrease cell viability. Particularly, NO decreased from 3716 ± 160 ppbv to 660 ± 107 ppbv, but NO₂ increased from 532 ± 44 ppbv to 2665 ± 43 ppbv, and O₃ increased from 22 ± 3 ppbv to 177 ± 32 ppbv (Table S4). In one study, 2500 ppbv of NO₂ exposure decreased viability of A549 cells to about 90% (Bakand et al. 2007). In another, 400 ppbv of O₃ exposure decreased cell viability to about 88% (Kosmider et al. 2010). These studies indicate that little of our observed decrease in cell viability is likely due to gas-phase NO₂ and O₃ and is primarily due to aged PM_{2.5} or could be due to co-exposure (synergistic) effects. The cell viability will be checked for gases (filtering air pollution sample through HEPA), particles, and their whole mixture (gas + particles) separately in the next FoxBox experiments to determine their individual and co-exposure effects (if any).

4. Conclusions and implications for environmental respiratory research

This study introduces the FoxBox, a large oxidative flow reactor at the Air Pollution Exposure Laboratory, and diagnoses its ability to simulate atmospheric aging of DE. It is capable of OH exposures up to 10^{12} molec cm⁻³ s, which is equivalent to almost 8 days in the atmosphere, with a flow rate 1300 to 2450 LPM that is necessary for eventual human exposure experiments. Its short residence times for gases and particles results in almost 100% transmission of particles of mobility diameters between 15 nm and 615 nm. The changes in DE particle size distributions and chemical composition with photochemical aging are consistent with those observed in the atmosphere and in other oxidative flow reactors. Thus, we have demonstrated that the FoxBox is capable of simulating, in a few minutes, many, if not most, of

the characteristics of DE aging in the atmosphere, signifying its suitability and applicability for aerosol aging studies in the APEL.

The vast majority of the global population is regularly exposed to levels of gases and PM_{2.5} exceeding WHO guidelines. It is noted that the chemical and physical characteristics of air pollutants change when they are transported long distances from their source locations to faraway locations due to atmospheric chemical processes, such as photochemical oxidation. Our preliminary study on cell viability found that photochemical aging significantly reduced cell viability, supporting observations that communities distant from air pollution sources are affected and vulnerable.

Controlled human exposure studies are a critical part of the set of interdisciplinary tools required to establish plausibility for the negative health effects of DE and other pollutant particles (Carlsten and Georas 2014). Yet the effects of inhaling more realistic photochemically aged aerosol particles has rarely been studied in controlled human exposures. This situation is concerning, especially given the potential of underappreciated health effects for communities exposed to photochemically aged particles. We contend that the integration of the FoxBox with a controlled human exposure system, albeit after a sufficient suite of tests at lower mass concentrations (to allow for a margin of safety) in our next set of *in vitro* experiments, will help address these concerns.

Acknowledgments

The authors thank Agnes Yuen, Cedric Chou, Carley Schwartz, and Andrew Lee for managerial and logistical support to the Air Pollution Exposure Laboratory. We are also grateful to the Vancouver Coastal Health Research Institute and The University of British Columbia for institutional support.

References

- Aerodyne (2019). PAM Users Manual. Aerodyne Research Inc., Billerica, MA.
- Akherati, A., He, Y., Coggon, M.M., Koss, A.R., Hodshire, A.L., Sekimoto, K., Warneke, C., De Gouw, J., Yee, L., Seinfeld, J.H., Onasch, T.B., Herndon, S.C., Knighton, W.B., Cappa, C.D., Kleeman, M.J., Lim, C.Y., Kroll, J.H., Pierce, J.R., and Jathar, S.H. (2020). Oxygenated Aromatic Compounds are Important Precursors of Secondary Organic Aerosol in Biomass-Burning Emissions. *Environ. Sci. Technol.* 54 (14):8568–8579. doi:10.1021/acs.est.0c01345.
- Aufderheide, M. (2005). Direct exposure methods for testing native atmospheres. *Exp. Toxicol. Pathol.* 57 (SUPPL. 1):213–226. doi:10.1016/j.etp.2005.05.019.
- Aufderheide, M., Halter, B., Möhle, N., and Hochrainer, D. (2013). The CULTEX RFS: A Comprehensive Technical Approach for the In Vitro Exposure of Airway Epithelial Cells to the Particulate Matter at the Air-Liquid Interface. *Biomed Res. Int.* 2013 (1):1–15. doi:10.1155/2013/734137.
- Bakand, S., Winder, C., and Hayes, A. (2007). Comparative in vitro cytotoxicity assessment of selected gaseous compounds in human alveolar epithelial cells. *Toxicol. Vitro* 21 (7):1341–1347. doi:10.1016/j.tiv.2007.04.013.
- Birger, N., Gould, T., Stewart, J., Miller, M.R., Larson, T., and Carlsten, C. (2011). The Air Pollution Exposure Laboratory (APEL) for controlled human exposure to diesel exhaust and other inhalants: Characterization and comparison to existing facilities. *Inhal. Toxicol.* 23 (4):219–225. doi:10.3109/08958378.2011.562256.
- Brauer, M., Freedman, G., Frostad, J., Van Donkelaar, A., Martin, R. V., Dentener, F., Dingenen, R. Van, Estep, K., Amini, H., Apte, J.S., Balakrishnan, K., Barregard, L., Broday, D., Feigin, V., Ghosh, S., Hopke, P.K., Knibbs, L.D., Kokubo, Y., Liu, Y., Ma, S., Morawska, L., Sangrador, J.L.T., Shaddick, G., Anderson, H.R., Vos, T., Forouzanfar, M.H., Burnett, R.T., and Cohen, A. (2016). Ambient Air Pollution Exposure Estimation for the Global Burden of Disease 2013. *Environ. Sci. Technol.* 50 (1):79–88. doi:10.1021/acs.est.5b03709.
- Brune, W.H. (2019). The Chamber Wall Index for Gas-Wall Interactions in Atmospheric Environmental Enclosures. *Environ. Sci. Technol.* 53 (7):3645–3652. doi:10.1021/acs.est.8b06260.
- Bruns, E.A., El Haddad, I., Keller, A., Klein, F., Kumar, N.K., Pieber, S.M., Corbin, J.C., Slowik, J.G., Brune, W.H., Baltensperger, U., and Prévôt, A.S.H. (2015). Inter-comparison of laboratory smog chamber and flow reactor systems on organic aerosol yield and composition. *Atmos. Meas. Tech.* 8 (6):2315–2332. doi:10.5194/amt-8-2315-2015.
- Canagaratna, M.R., Jimenez, J.L., Kroll, J.H., Chen, Q., Kessler, S.H., Massoli, P., Hildebrandt Ruiz, L., Fortner, E., Williams, L.R., Wilson, K.R., Surratt, J.D., Donahue, N.M., Jayne, J.T., and Worsnop, D.R. (2015). Elemental ratio measurements of organic compounds using aerosol mass spectrometry: Characterization, improved calibration, and implications. *Atmos. Chem. Phys.* 15 (1):253–272. doi:10.5194/acp-15-253-2015.
- Cao, J., Wang, Q., Li, L., Zhang, Y., Tian, J., Chen, L.W.A., Ho, S.S.H., Wang, X., Chow, J.C., and Watson, J.G. (2020). Evaluation of the Oxidation Flow Reactor for particulate matter emission limit certification. *Atmos. Environ.* 224 (November 2019). doi:10.1016/j.atmosenv.2019.117086.

- Carlsten, C. and Georas, S.N. (2014). Update in environmental and occupational lung diseases 2013. *Am. J. Respir. Crit. Care Med.* 189 (9):1037–1043. doi:10.1164/rccm.201401-0108UP.
- Choudhary, V., Mandariya, A.K., Zhao, R., and Gupta, T. (2024). Field evidence of brown carbon absorption enhancement linked to organic nitrogen formation in Indo-Gangetic Plain. *Sci. Total Environ.* 930 (August 2023):172506. doi:10.1016/j.scitotenv.2024.172506.
- Chowdhury, P.H., He, Q., Lasitza Male, T., Brune, W.H., Rudich, Y., and Pardo, M. (2018). Exposure of Lung Epithelial Cells to Photochemically Aged Secondary Organic Aerosol Shows Increased Toxic Effects. *Environ. Sci. Technol. Lett.* 5 (7):424–430. doi:10.1021/acs.estlett.8b00256.
- Cohen, A.J., Brauer, M., Burnett, R., Anderson, H.R., Frostad, J., Estep, K., Balakrishnan, K., Brunekreef, B., Dandona, L., Dandona, R., Feigin, V., Freedman, G., Hubbell, B., Jobling, A., Kan, H., Knibbs, L., Liu, Y., Martin, R., Morawska, L., Pope, C.A., Shin, H., Straif, K., Shaddick, G., Thomas, M., van Dingenen, R., van Donkelaar, A., Vos, T., Murray, C.J.L., and Forouzanfar, M.H. (2017). Estimates and 25-year trends of the global burden of disease attributable to ambient air pollution: an analysis of data from the Global Burden of Diseases Study 2015. *Lancet* 389 (10082):1907–1918. doi:10.1016/S0140-6736(17)30505-6.
- Cubison, M.J., Ortega, A.M., Hayes, P.L., Farmer, D.K., Day, D., Lechner, M.J., Brune, W.H., Apel, E., Diskin, G.S., Fisher, J.A., Fuelberg, H.E., Hecobian, A., Knapp, D.J., Mikoviny, T., Riemer, D., Sachse, G.W., Sessions, W., Weber, R.J., Weinheimer, A.J., Wisthaler, A., and Jimenez, J.L. (2011). Effects of aging on organic aerosol from open biomass burning smoke in aircraft and laboratory studies. *Atmos. Chem. Phys.* 11 (23):12049–12064. doi:10.5194/acp-11-12049-2011.
- DeCarlo, P.F., Kimmel, J.R., Trimborn, A., Northway, M.J., Jayne, J.T., Aiken, A.C., Gonin, M., Fuhrer, K., Horvath, T., Docherty, K.S., Worsnop, D.R., and Jimenez, J.L. (2006). Field-deployable, high-resolution, time-of-flight aerosol mass spectrometer. *Anal. Chem.* 78 (24):8281–8289. doi:10.1021/ac061249n.
- Delfino, R.J., Staimer, N., Tjoa, T., Arhami, M., Polidori, A., Gillen, D.L., George, S.C., Shafer, M.M., Schauer, J.J., and Sioutas, C. (2010). Associations of primary and secondary organic aerosols with airway and systemic inflammation in an elderly panel cohort. *Epidemiology* 21 (6):892–902. doi:10.1097/EDE.0b013e3181f20e6c.
- Donahue, N.M., Robinson, A.L., Stanier, C.O., and Pandis, S.N. (2006). Coupled partitioning, dilution, and chemical aging of semivolatile organics. *Environ. Sci. Technol.* 40 (8):2635–2643. doi:10.1021/es052297c.
- Ervens, B. (2015). Modeling the Processing of Aerosol and Trace Gases in Clouds and Fogs. *Chem. Rev.* 115 (10):4157–4198. doi:10.1021/cr5005887.
- Ervens, B., Turpin, B.J., and Weber, R.J. (2011). Secondary organic aerosol formation in cloud droplets and aqueous particles (aqSOA): A review of laboratory, field and model studies. *Atmos. Chem. Phys.* 11 (21):11069–11102. doi:10.5194/acp-11-11069-2011.
- Ezell, M.J., Johnson, S.N., Yu, Y., Perraud, V., Bruns, E.A., Alexander, M.L., Zelenyuk, A., Dabdub, D., and Finlayson-Pitts, B.J. (2010). A new aerosol flow system for photochemical and thermal studies of tropospheric aerosols. *Aerosol Sci. Technol.* 44

(5):329–338. doi:10.1080/02786821003639700.

- Fogler, H.S. and Gürmen, M.N. (1999). Elements of Chemical Reaction Engineering. 2005. *Search PubMed* 813–866.
- George, I.J., Vlasenko, A., Slowik, J.G., Broekhuizen, K., and Abbatt, J.P.D. (2007). Heterogeneous oxidation of saturated organic aerosols by hydroxyl radicals: Uptake kinetics, condensed-phase products, and particle size change. *Atmos. Chem. Phys.* 7 (16):4187–4201. doi:10.5194/acp-7-4187-2007.
- Guo, S., Hu, M., Peng, J., Wu, Z., Zamora, M.L., Shang, D., Du, Z., Zheng, J., Fang, X., Tang, R., Wu, Y., Zeng, L., Shuai, S., Zhang, W., Wang, Y., Ji, Y., Li, Y., Zhang, A.L., Wang, W., Zhang, F., Zhao, J., Gong, X., Wang, C., Molina, M.J., and Zhang, R. (2020). Remarkable nucleation and growth of ultrafine particles from vehicular exhaust. *Proc. Natl. Acad. Sci. U. S. A.* 117 (7):3427–3432. doi:10.1073/pnas.1916366117.
- Hallquist, M., Wenger, J.C., Baltensperger, U., Rudich, Y., Simpson, D., Claeys, M., Dommen, J., Donahue, N.M., George, C., Goldstein, A.H., Hamilton, J.F., Herrmann, H., Hoffmann, T., Iinuma, Y., Jang, M., Jenkin, M.E., Jimenez, J.L., Kiendler-Scharr, A., Maenhaut, W., McFiggans, G., Mentel, T.F., Monod, A., Prévôt, A.S.H., Seinfeld, J.H., Surratt, J.D., Szmigielski, R., and Wildt, J. (2009). The formation, properties and impact of secondary organic aerosol: Current and emerging issues. *Atmos. Chem. Phys.* 9 (14):5155–5236. doi:10.5194/acp-9-5155-2009.
- Hansen, M.B., Nielsen, S.E., and Berg, K. (1989). Re-examination and further development of a precise and rapid dye method for measuring cell growth/cell kill. *J. Immunol. Methods* 119 (2):203–210. doi:10.1016/0022-1759(89)90397-9.
- Hayes, P.L., Ortega, A.M., Cubison, M.J., Froyd, K.D., Zhao, Y., Cliff, S.S., Hu, W.W., Toohey, D.W., Flynn, J.H., Lefer, B.L., Grossberg, N., Alvarez, S., Rappenglück, B., Taylor, J.W., Allan, J.D., Holloway, J.S., Gilman, J.B., Kuster, W.C., De Gouw, J.A., Massoli, P., Zhang, X., Liu, J., Weber, R.J., Corrigan, A.L., Russell, L.M., Isaacman, G., Worton, D.R., Kreisberg, N.M., Goldstein, A.H., Thalman, R., Waxman, E.M., Volkamer, R., Lin, Y.H., Surratt, J.D., Kleindienst, T.E., Offenberg, J.H., Dusanter, S., Griffith, S., Stevens, P.S., Brioude, J., Angevine, W.M., and Jimenez, J.L. (2013). Organic aerosol composition and sources in Pasadena, California, during the 2010 CalNex campaign. *J. Geophys. Res. Atmos.* 118 (16):9233–9257. doi:10.1002/jgrd.50530.
- Heald, C.L., Kroll, J.H., Jimenez, J.L., Docherty, K.S., Decarlo, P.F., Aiken, A.C., Chen, Q., Martin, S.T., Farmer, D.K., and Artaxo, P. (2010). A simplified description of the evolution of organic aerosol composition in the atmosphere. *Geophys. Res. Lett.* 37 (8). doi:10.1029/2010GL042737.
- Huang, Y., Coggon, M.M., Zhao, R., Lignell, H., Bauer, M.U., Flagan, R.C., and Seinfeld, J.H. (2017). The Caltech Photooxidation Flow Tube reactor: Design, fluid dynamics and characterization. *Atmos. Meas. Tech.* 10 (3):839–867. doi:10.5194/amt-10-839-2017.
- Ihalainen, M., Tiitta, P., Czech, H., Yli-Pirilä, P., Hartikainen, A., Kortelainen, M., Tissari, J., Stengel, B., Sklorz, M., Suhonen, H., Lamberg, H., Leskinen, A., Kiendler-Scharr, A., Harndorf, H., Zimmermann, R., Jokiniemi, J., and Sippula, O. (2019). A novel high-volume Photochemical Emission Aging flow tube Reactor (PEAR). *Aerosol Sci. Technol.* 53 (3):276–294. doi:10.1080/02786826.2018.1559918.
- Jimenez, J.L., Canagaratna, M.R., Donahue, N.M., Prevot, A.S.H., Zhang, Q., Kroll, J.H.,

- DeCarlo, P.F., Allan, J.D., Coe, H., Ng, N.L., Aiken, A.C., Docherty, K.S., Ulbrich, I.M., Grieshop, A.P., Robinson, A.L., Duplissy, J., Smith, J.D., Wilson, K.R., Lanz, V.A., Hueglin, C., Sun, Y.L., Tian, J., Laaksonen, A., Raatikainen, T., Rautiainen, J., Vaattovaara, P., Ehn, M., Kulmala, M., Tomlinson, J.M., Collins, D.R., Cubison, M.J., Dunlea, E.J., Huffman, J.A., Onasch, T.B., Alfarra, M.R., Williams, P.I., Bower, K., Kondo, Y., Schneider, J., Drewnick, F., Borrmann, S., Weimer, S., Demerjian, K., Salcedo, D., Cottrell, L., Griffin, R., Takami, A., Miyoshi, T., Hatakeyama, S., Shimono, A., Sun, J.Y., Zhang, Y.M., Dzepina, K., Kimmel, J.R., Sueper, D., Jayne, J.T., Herndon, S.C., Trimborn, A.M., Williams, L.R., Wood, E.C., Middlebrook, A.M., Kolb, C.E., Baltensperger, U., and Worsnop, D.R. (2009). Evolution of organic aerosols in the atmosphere. *Science* (80-.). 326 (5959):1525–1529. doi:10.1126/science.1180353.
- Jimenez, J.L., Jayne, J.T., Shi, Q., Kolb, C.E., Worsnop, D.R., Yourshaw, I., Seinfeld, J.H., Flagan, R.C., Zhang, X., Smith, K.A., Morris, J.W., and Davidovits, P. (2003). Ambient aerosol sampling using the Aerodyne aerosol mass spectrometer. *J. Geophys. Res. Atmos.* 108 (7):1–13. doi:10.1029/2001jd001213.
- Kan, C.S., Calvert, J.G., and Shaw, J.H. (1981). Oxidation of sulfur dioxide by methylperoxy radicals. *J. Phys. Chem.* 85 (9):1126–1132. doi:10.1021/j150609a011.
- Kanakidou, M., Seinfeld, J.H., Pandis, S.N., Barnes, I., Dentener, F.J., Facchini, M.C., Van Dingenen, R., Ervens, B., Nenes, A., Nielsen, C.J., Swietlicki, E., Putaud, J.P., Balkanski, Y., Fuzzi, S., Horth, J., Moortgat, G.K., Winterhalter, R., Myhre, C.E.L., Tsigaridis, K., Vignati, E., Stephanou, E.G., and Wilson, J. (2005). Organic aerosol and global climate modelling: A review. *Atmos. Chem. Phys.* 5 (4):1053–1123. doi:10.5194/acp-5-1053-2005.
- Kang, E., Root, M.J., Toohey, D.W., and Brune, W.H. (2007). Introducing the concept of Potential Aerosol Mass (PAM). *Atmos. Chem. Phys.* 7 (22):5727–5744. doi:10.5194/acp-7-5727-2007.
- Keller, A. and Bartsch, H. (2012). A continuous photo-oxidation flow reactor for a defined measurement of the SOA formation potential of wood burning emissions. *J. Aerosol Sci.* 49:9–20. doi:10.1016/j.jaerosci.2012.02.007.
- Knote, C., Hodzic, A., and Jimenez, J.L. (2015). The effect of dry and wet deposition of condensable vapors on secondary organic aerosols concentrations over the continental US. *Atmos. Chem. Phys.* 15 (1):1–18. doi:10.5194/acp-15-1-2015.
- Kosmider, B., Loader, J.E., Murphy, R.C., and Mason, R.J. (2010). Apoptosis induced by ozone and oxysterols in human alveolar epithelial cells. *Free Radic. Biol. Med.* 48 (11):1513–1524. doi:10.1016/j.freeradbiomed.2010.02.032.
- Krechmer, J.E., Coggon, M.M., Massoli, P., Nguyen, T.B., Crounse, J.D., Hu, W., Day, D.A., Tyndall, G.S., Henze, D.K., Rivera-Rios, J.C., Nowak, J.B., Kimmel, J.R., Mauldin, R.L., Stark, H., Jayne, J.T., Sipilä, M., Junninen, H., St. Clair, J.M., Zhang, X., Feiner, P.A., Zhang, L., Miller, D.O., Brune, W.H., Keutsch, F.N., Wennberg, P.O., Seinfeld, J.H., Worsnop, D.R., Jimenez, J.L., and Canagaratna, M.R. (2015). Formation of Low Volatility Organic Compounds and Secondary Organic Aerosol from Isoprene Hydroxyhydroperoxide Low-NO Oxidation. *Environ. Sci. Technol.* 49 (17):10330–10339. doi:10.1021/acs.est.5b02031.
- Krechmer, J.E., Pagonis, D., Ziemann, P.J., and Jimenez, J.L. (2016). Quantification of Gas-Wall Partitioning in Teflon Environmental Chambers Using Rapid Bursts of Low-

Volatility Oxidized Species Generated in Situ. *Environ. Sci. Technol.* 50 (11):5757–5765. doi:10.1021/acs.est.6b00606.

- Kutz, M. (2012). *Handbook of Environmental Degradation of Materials* (Second Edition), William Andrew Publishing. Elsevier, Oxford.
- Lambe, A.T., Ahern, A.T., Williams, L.R., Slowik, J.G., Wong, J.P.S., Abbatt, J.P.D., Brune, W.H., Ng, N.L., Wright, J.P., Croasdale, D.R., Worsnop, D.R., Davidovits, P., and Onasch, T.B. (2011). Characterization of aerosol photooxidation flow reactors: Heterogeneous oxidation, secondary organic aerosol formation and cloud condensation nuclei activity measurements. *Atmos. Meas. Tech.* 4 (3):445–461. doi:10.5194/amt-4-445-2011.
- Lambe, A.T., Chhabra, P.S., Onasch, T.B., Brune, W.H., Hunter, J.F., Kroll, J.H., Cummings, M.J., Brogan, J.F., Parmar, Y., Worsnop, D.R., Kolb, C.E., and Davidovits, P. (2015). Effect of oxidant concentration, exposure time, and seed particles on secondary organic aerosol chemical composition and yield. *Atmos. Chem. Phys.* 15 (6):3063–3075. doi:10.5194/acp-15-3063-2015.
- Lambe, A.T., Onasch, T.B., Croasdale, D.R., Wright, J.P., Martin, A.T., Franklin, J.P., Massoli, P., Kroll, J.H., Canagaratna, M.R., Brune, W.H., Worsnop, D.R., and Davidovits, P. (2012). Transitions from functionalization to fragmentation reactions of laboratory Secondary Organic Aerosol (SOA) generated from the OH oxidation of alkane precursors. *Environ. Sci. Technol.* 46 (10):5430–5437. doi:10.1021/es300274t.
- Lee Ng, N., Brown, S.S., Archibald, A.T., Atlas, E., Cohen, R.C., Crowley, J.N., Day, D.A., Donahue, N.M., Fry, J.L., Fuchs, H., Griffin, R.J., Guzman, M.I., Herrmann, H., Hodzic, A., Iinuma, Y., Kiendler-Scharr, A., Lee, B.H., Luecken, D.J., Mao, J., McLaren, R., Mutzel, A., Osthoff, H.D., Ouyang, B., Picquet-Varrault, B., Platt, U., Pye, H.O.T., Rudich, Y., Schwantes, R.H., Shiraiwa, M., Stutz, J., Thornton, J.A., Tilgner, A., Williams, B.J., and Zaveri, R.A. (2017). Nitrate radicals and biogenic volatile organic compounds: Oxidation, mechanisms, and organic aerosol. *Atmos. Chem. Phys.* 17 (3):2103–2162. doi:10.5194/acp-17-2103-2017.
- Li, R., Palm, B.B., Ortega, A.M., Hlywiak, J., Hu, W., Peng, Z., Day, D.A., Knote, C., Brune, W.H., De Gouw, J.A., and Jimenez, J.L. (2015). Modeling the radical chemistry in an oxidation flow reactor: Radical formation and recycling, sensitivities, and the OH exposure estimation equation. *J. Phys. Chem. A* 119 (19):4418–4432. doi:10.1021/jp509534k.
- Lim, Y.B., Tan, Y., Perri, M.J., Seitzinger, S.P., and Turpin, B.J. (2010). Aqueous chemistry and its role in secondary organic aerosol (SOA) formation. *Atmos. Chem. Phys.* 10 (21):10521–10539. doi:10.5194/acp-10-10521-2010.
- Long, E., Schwartz, C., and Carlsten, C. (2022). Controlled human exposure to diesel exhaust: a method for understanding health effects of traffic-related air pollution. *Part. Fibre Toxicol.* 19 (1):1–22. doi:10.1186/s12989-022-00454-1.
- Longhin, E., Gualtieri, M., Capasso, L., Bengalli, R., Møllerup, S., Holme, J.A., Øvrevik, J., Casadei, S., Di Benedetto, C., Parenti, P., and Camatini, M. (2016). Physico-chemical properties and biological effects of diesel and biomass particles. *Environ. Pollut.* 215:366–375. doi:10.1016/j.envpol.2016.05.015.
- Mao, J., Ren, X., Brune, W.H., Olson, J.R., Crawford, J.H., Fried, A., Huey, L.G., Cohen, R.C.,

- Heikes, B., Singh, H.B., Blake, D.R., Sachse, G.W., Diskin, G.S., Hall, S.R., and Shetter, R.E. (2009). Airborne measurement of OH reactivity during INTEx-B. *Atmos. Chem. Phys.* 9 (1):163–173. doi:10.5194/acp-9-163-2009.
- McCarthy, C.E., Duffney, P.F., Wyatt, J.D., Thatcher, T.H., Phipps, R.P., and Sime, P.J. (2017). Comparison of in vitro toxicological effects of biomass smoke from different sources of animal dung. *Toxicol. Vitro.* 43:76–86. doi:10.1016/j.tiv.2017.05.021.
- Mentel, T.F., Bleilebens, D., and Wahner, A. (1996). A study of nighttime nitrogen oxide oxidation in a large reaction chamber - The fate of NO₂, N₂O₅, HNO₃, and O₃ at different humidities. *Atmos. Environ.* 30 (23):4007–4020. doi:10.1016/1352-2310(96)00117-3.
- Mills, N.L., Törnqvist, H., Gonzalez, M.C., Vink, E., Robinson, S.D., Söderberg, S., Boon, N.A., Donaldson, K., Sandström, T., Blomberg, A., and Newby, D.E. (2007). Ischemic and Thrombotic Effects of Dilute Diesel-Exhaust Inhalation in Men with Coronary Heart Disease. *N. Engl. J. Med.* 357 (11):1075–1082. doi:10.1056/nejmoa066314.
- Ng, N.L., Canagaratna, M.R., Jimenez, J.L., Chhabra, P.S., Seinfeld, J.H., and Worsnop, D.R. (2011). Changes in organic aerosol composition with aging inferred from aerosol mass spectra. *Atmos. Chem. Phys.* 11 (13):6465–6474. doi:10.5194/acp-11-6465-2011.
- Ng, N.L., Canagaratna, M.R., Zhang, Q., Jimenez, J.L., Tian, J., Ulbrich, I.M., Kroll, J.H., Docherty, K.S., Chhabra, P.S., Bahreini, R., Murphy, S.M., Seinfeld, J.H., Hildebrandt, L., Donahue, N.M., Decarlo, P.F., Lanz, V.A., Prévôt, A.S.H., Dinar, E., Rudich, Y., and Worsnop, D.R. (2010). Organic aerosol components observed in Northern Hemispheric datasets from Aerosol Mass Spectrometry. *Atmos. Chem. Phys.* 10 (10):4625–4641. doi:10.5194/acp-10-4625-2010.
- Nguyen, T.B., Crounse, J.D., Teng, A.P., Clair, J.M.S., Paulot, F., Wolfe, G.M., and Wennberg, P.O. (2015). Rapid deposition of oxidized biogenic compounds to a temperate forest. *Proc. Natl. Acad. Sci. U. S. A.* 112 (5):E392–E401. doi:10.1073/pnas.1418702112.
- Nordenhäll, C., Pourazar, J., Blomberg, A., Levin, J.O., Sandström, T., and Ädelroth, E. (2000). Airway inflammation following exposure to diesel exhaust: A study of time kinetics using induced sputum. *Eur. Respir. J.* 15 (6):1046–1051. doi:10.1034/j.1399-3003.2000.01512.x.
- Odum, J.R., Jungkamp, T.P.W., Griffin, R.J., Flagan, R.C., and Seinfeld, J.H. (1997). The atmospheric aerosol-forming potential of whole gasoline vapor. *Science* (80-.). 276 (5309):96–99. doi:10.1126/science.276.5309.96.
- Ortega, A.M., Day, D.A., Cubison, M.J., Brune, W.H., Bon, D., De Gouw, J.A., and Jimenez, J.L. (2013). Secondary organic aerosol formation and primary organic aerosol oxidation from biomass-burning smoke in a flow reactor during FLAME-3. *Atmos. Chem. Phys.* 13 (22):11551–11571. doi:10.5194/acp-13-11551-2013.
- Palm, B.B., Campuzano-Jost, P., Ortega, A.M., Day, D.A., Kaser, L., Jud, W., Karl, T., Hansel, A., Hunter, J.F., Cross, E.S., Kroll, J.H., Peng, Z., Brune, W.H., and Jimenez, J.L. (2016). In situ secondary organic aerosol formation from ambient pine forest air using an oxidation flow reactor. *Atmos. Chem. Phys.* 16 (5):2943–2970. doi:10.5194/acp-16-2943-2016.
- PAM Wiki (2024). Available at <https://sites.google.com/site/pamwiki/>.
- Pang, Y., Huang, W., Luo, X.-S., Chen, Q., Zhao, Z., Tang, M., Hong, Y., Chen, J., and Li, H.

- (2020). In-vitro human lung cell injuries induced by urban PM_{2.5} during a severe air pollution episode: Variations associated with particle components. *Ecotoxicol. Environ. Saf.* 206:111406. doi:10.1016/j.ecoenv.2020.111406.
- Pankow, J.F. (1994). An absorption model of gas/particle partitioning of organic compounds in the atmosphere. *Atmos. Environ.* 28 (2):185–188. doi:10.1016/1352-2310(94)90093-0.
- Papapostolou, V., Lawrence, J.E., Ferguson, S.T., Wolfson, J.M., Diaz, E.A., Godleski, J.J., and Koutrakis, P. (2013). Development and characterization of an exposure generation system to investigate the health effects of particles from fresh and aged traffic emissions. *Air Qual. Atmos. Heal.* 6 (2):419–429. doi:10.1007/s11869-012-0178-3.
- Pathak, R.K., Stanier, C.O., Donahue, N.M., and Pandis, S.N. (2007). Ozonolysis of α -pinene at atmospherically relevant concentrations: Temperature dependence of aerosol mass fractions (yields). *J. Geophys. Res. Atmos.* 112 (D3). doi:10.1029/2006JD007436.
- Peng, Z., Day, D.A., Ortega, A.M., Palm, B.B., Hu, W., Stark, H., Li, R., Tsigaridis, K., Brune, W.H., and Jimenez, J.L. (2016). Non-OH chemistry in oxidation flow reactors for the study of atmospheric chemistry systematically examined by modeling. *Atmos. Chem. Phys.* 16 (7):4283–4305. doi:10.5194/acp-16-4283-2016.
- Peng, Z., Day, D.A., Stark, H., Li, R., Lee-Taylor, J., Palm, B.B., Brune, W.H., and Jimenez, J.L. (2015). HO_x radical chemistry in oxidation flow reactors with low-pressure mercury lamps systematically examined by modeling. *Atmos. Meas. Tech.* 8 (11):4863–4890. doi:10.5194/amt-8-4863-2015.
- Peng, Z. and Jimenez, J.L. (2020). Radical chemistry in oxidation flow reactors for atmospheric chemistry research. *Chem. Soc. Rev.* 49 (9):2570–2616. doi:10.1039/c9cs00766k.
- Peretz, A., Kaufman, J.D., Trenga, C.A., Allen, J., Carlsten, C., Aulet, M.R., Adar, S.D., and Sullivan, J.H. (2008). Effects of diesel exhaust inhalation on heart rate variability in human volunteers. *Environ. Res.* 107 (2):178–184. doi:10.1016/j.envres.2008.01.012.
- Pope, C.A. and Dockery, D.W. (2006). Health effects of fine particulate air pollution: Lines that connect. *J. Air Waste Manag. Assoc.* 56 (6):709–742. doi:10.1080/10473289.2006.10464485.
- Pöschl, U. (2005). Atmospheric aerosols: Composition, transformation, climate and health effects. *Angew. Chemie - Int. Ed.* 44 (46):7520–7540. doi:10.1002/anie.200501122.
- Presto, A.A., Gordon, T.D., and Robinson, A.L. (2014). Primary to secondary organic aerosol: Evolution of organic emissions from mobile combustion sources. *Atmos. Chem. Phys.* 14 (10):5015–5036. doi:10.5194/acp-14-5015-2014.
- Rajeev, P., Choudhary, V., Chakraborty, A., Singh, G.K., and Gupta, T. (2022). Light absorption potential of water-soluble organic aerosols in the two polluted urban locations in the central Indo-Gangetic Plain. *Environ. Pollut.* 314. doi:10.1016/j.envpol.2022.120228.
- Richards-Henderson, N.K., Goldstein, A.H., and Wilson, K.R. (2016). Sulfur Dioxide Accelerates the Heterogeneous Oxidation Rate of Organic Aerosol by Hydroxyl Radicals. *Environ. Sci. Technol.* 50 (7):3554–3561. doi:10.1021/acs.est.5b05369.
- Rider, C.F., Yamamoto, M., Günther, O.P., Hirota, J.A., Singh, A., Tebbutt, S.J., and Carlsten, C. (2016). Controlled diesel exhaust and allergen coexposure modulates microRNA and gene expression in humans: Effects on inflammatory lung markers. *J. Allergy Clin.*

- Immunol.* 138 (6):1690–1700. doi:10.1016/j.jaci.2016.02.038.
- Roig Rodelas, R., Chakraborty, A., Perdrix, E., Tison, E., and Riffault, V. (2019). Real-time assessment of wintertime organic aerosol characteristics and sources at a suburban site in northern France. *Atmos. Environ.* 203 (June 2018):48–61. doi:10.1016/j.atmosenv.2019.01.035.
- Rossner, P., Cervena, T., and Vojtisek-Lom, M. (2021). In vitro exposure to complete engine emissions – a mini-review. *Toxicology* 462:152953. doi:10.1016/j.tox.2021.152953.
- Sander, S.P., Friedl, R.R., Abbatt, J., Barker, J.R., Burkholder, J.B., Kolb, C.E., Kurylo, M.J., Moortgat, G.K., Wine, P.H., Huie, R.E., and Orkin, V.L. (2011). Chemical kinetics and photochemical data for use in atmospheric studies: Evaluation number 17, *Jet Propulsion Laboratory*.
- Schuck, E.A. and Rogers, L.H. (1959). Eye irritation from irradiated automobile exhaust (effect of irradiation intensity; half-life studies). *J. Air Pollut. Control Assoc.* 8 (4):310–313. doi:10.1080/00022470.1959.10467858.
- Simonen, P., Saukko, E., Karjalainen, P., Timonen, H., Bloss, M., Aakko-Saksa, P., Rönkkö, T., Keskinen, J., and Dal Maso, M. (2017). A new oxidation flow reactor for measuring secondary aerosol formation of rapidly changing emission sources. *Atmos. Meas. Tech.* 10 (4):1519–1537. doi:10.5194/amt-10-1519-2017.
- Srivastava, D., Vu, T. V., Tong, S., Shi, Z., and Harrison, R.M. (2022). Formation of secondary organic aerosols from anthropogenic precursors in laboratory studies. *npj Clim. Atmos. Sci.* 5 (1). doi:10.1038/s41612-022-00238-6.
- Wang, B., Chen, H., Xenaki, D., Liao, J., Cowie, C., and Oliver, B.G. (2021). Differential inflammatory and toxic effects in-vitro of wood smoke and traffic-related particulate matter from Sydney, Australia. *Chemosphere*.
- Wang, H., Guo, S., Wu, Z., Qiao, K., Tang, R., Yu, Y., Xu, W., Zhu, W., Zeng, L., Huang, X., He, L., and Hallquist, M. (2022). Secondary organic aerosol formation from straw burning using an oxidation flow reactor. *J. Environ. Sci. (China)* 114:249–258. doi:10.1016/j.jes.2021.08.049.
- Weitekamp, C.A., Stevens, T., Stewart, M.J., Bhawe, P., and Gilmour, M.I. (2020). Health effects from freshly emitted versus oxidatively or photochemically aged air pollutants. *Sci. Total Environ.* 704:135772. doi:10.1016/j.scitotenv.2019.135772.
- Weitkamp, E.A., Sage, A.M., Pierce, J.R., Donahue, N.M., and Robinson, A.L. (2007). Organic aerosol formation from photochemical oxidation of diesel exhaust in a smog chamber. *Environ. Sci. Technol.* 41 (20):6969–6975. doi:10.1021/es070193r.
- Wu, C., Brown, R.A., Brown, Z.E., Trounce, H., Horchler, E.J., Wang, L., Miljevic, B., Zhang, C., Wang, H., Wang, B., Ristovski, Z., and Stevanovic, S. (2023). A new oxidation flow reactor for the measurements of secondary aerosol formation: Characterisation and a case study. *Atmos. Environ.* 309 (December 2022):119886. doi:10.1016/j.atmosenv.2023.119886.
- Wu, S., Lü, Z., Hao, J., Zhao, Z., Li, J., Takekawa, H., Minoura, H., and Yasuda, A. (2007). Construction and characterization of an atmospheric simulation smog chamber. *Adv. Atmos. Sci.* 24 (2):250–258. doi:10.1007/s00376-007-0250-3.
- Wu, W., Jin, Y., and Carlsten, C. (2018). Inflammatory health effects of indoor and outdoor

- particulate matter. *J. Allergy Clin. Immunol.* 141 (3):833–844. doi:10.1016/j.jaci.2017.12.981.
- Xu, N. and Collins, D.R. (2021). Design and characterization of a new oxidation flow reactor for laboratory and long-term ambient studies. *Atmos. Meas. Tech.* 14 (4):2891–2906. doi:10.5194/amt-14-2891-2021.
- Yazdani, A., Dudani, N., Takahama, S., Bertrand, A., Prévôt, A.S.H., El Haddad, I., and Dillner, A.M. (2021). Characterization of primary and aged wood burning and coal combustion organic aerosols in an environmental chamber and its implications for atmospheric aerosols. *Atmos. Chem. Phys.* 21 (13):10273–10293. doi:10.5194/acp-21-10273-2021.
- Ye, P., Ding, X., Hakala, J., Hofbauer, V., Robinson, E.S., and Donahue, N.M. (2016). Vapor wall loss of semi-volatile organic compounds in a Teflon chamber. *Aerosol Sci. Technol.* 50 (8):822–834. doi:10.1080/02786826.2016.1195905.
- Ylisirniö, A., Buchholz, A., Mohr, C., Li, Z., Barreira, L., Lambe, A., Faiola, C., Kari, E., Yli-Juuti, T., Nizkorodov, S.A., Worsnop, D.R., Virtanen, A., and Schobesberger, S. (2020). Composition and volatility of secondary organic aerosol (SOA) formed from oxidation of real tree emissions compared to simplified volatile organic compound (VOC) systems. *Atmos. Chem. Phys.* 20 (9):5629–5644. doi:10.5194/acp-20-5629-2020.
- Yu, Z., Jang, M., Sabo-Attwood, T., Robinson, S.E., and Jiang, H. (2017). Prediction of delivery of organic aerosols onto air-liquid interface cells in vitro using an electrostatic precipitator. *Toxicol. Vitr.* 42 (April):319–328. doi:10.1016/j.tiv.2017.05.011.
- Zhang, Y., Seigneur, C., Seinfeld, J.H., Jacobson, M., Clegg, S.L., and Binkowski, F.S. (2000). A comparative review of inorganic aerosol thermodynamic equilibrium modules: Similarities, differences, and their likely causes. *Atmos. Environ.* 34 (1):117–137. doi:10.1016/S1352-2310(99)00236-8.
- Zhao, R., Lee, A.K.Y., Huang, L., Li, X., Yang, F., and Abbatt, J.P.D. (2015). Photochemical processing of aqueous atmospheric brown carbon. *Atmos. Chem. Phys.* 15 (11):6087–6100. doi:10.5194/acp-15-6087-2015.
- Zhao, R., Zhang, Q., Xu, X., Zhao, W., Yu, H., Wang, W., Zhang, Y., and Zhang, W. (2021). Effect of experimental conditions on secondary organic aerosol formation in an oxidation flow reactor. *Atmos. Pollut. Res.* 12 (3):205–213. doi:10.1016/j.apr.2021.01.011.

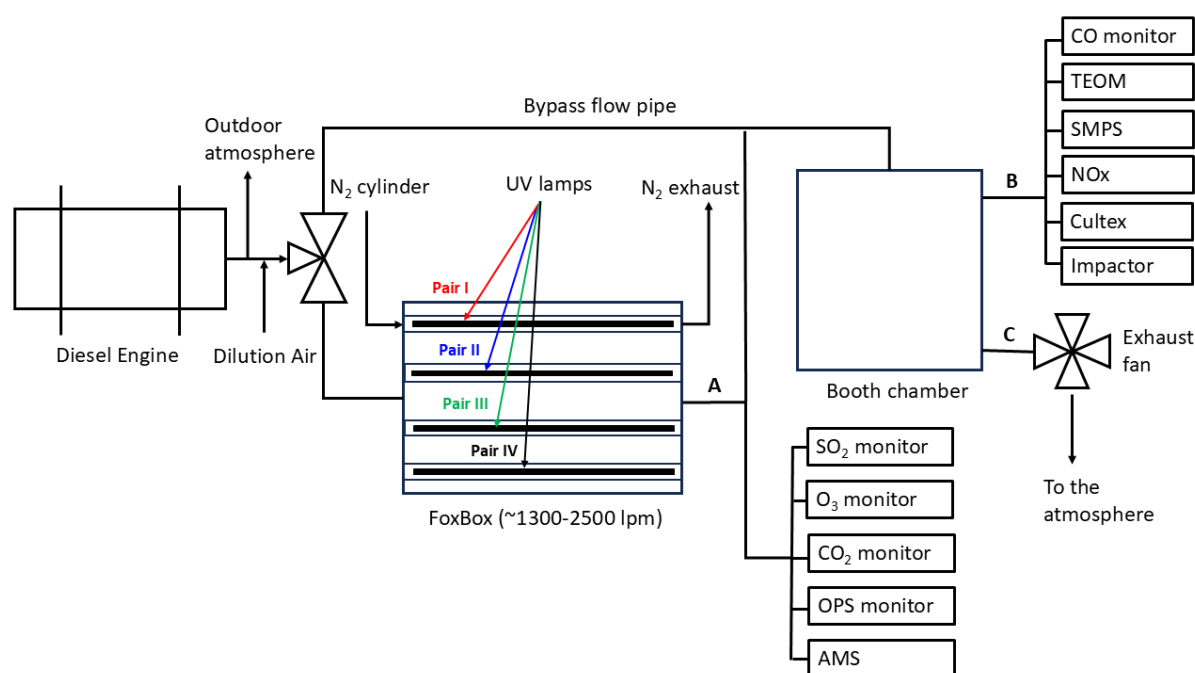


Fig. 1. Schematic diagram of the experimental setup used in this study. The engine produces a large amount of exhaust through an engine exhaust line, most of which is unnecessary for experiments and thus, vented to the outdoor atmosphere. A small portion of diluted diesel exhaust (DE) was fed into the booth directly (via the bypass flow pipe) and via the FoxBox, with a 3-way valve placed upstream to switch flows. A number of gas and particle monitors were operated at the FoxBox exit (point A) and booth exit (point B). Point C is the location where exhaust flow rates were measured.

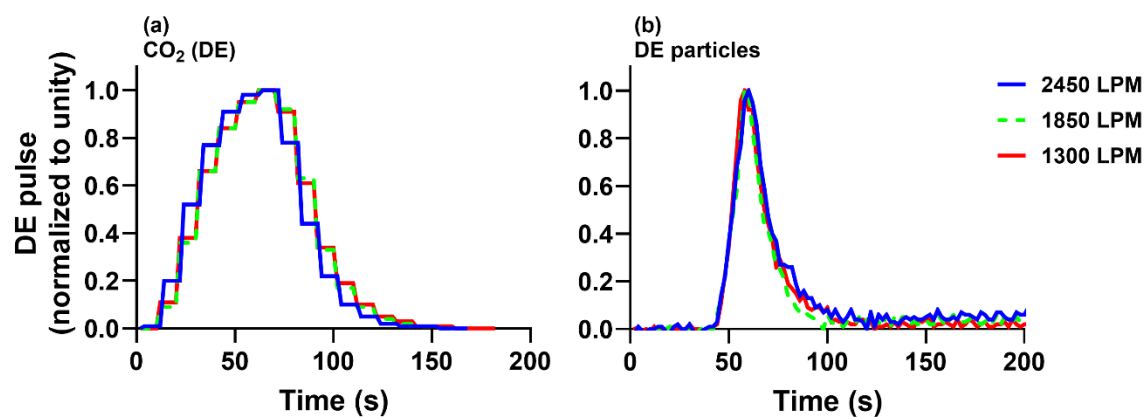


Fig. 2. Residence time distribution (RTD) measurements of: (a) CO₂, and (b) particles in twenty-second pulses of DE (normalized to pulse height), at the immediate outlet of the FoxBox, at different flow rates. UV lamps were turned off during these measurements.

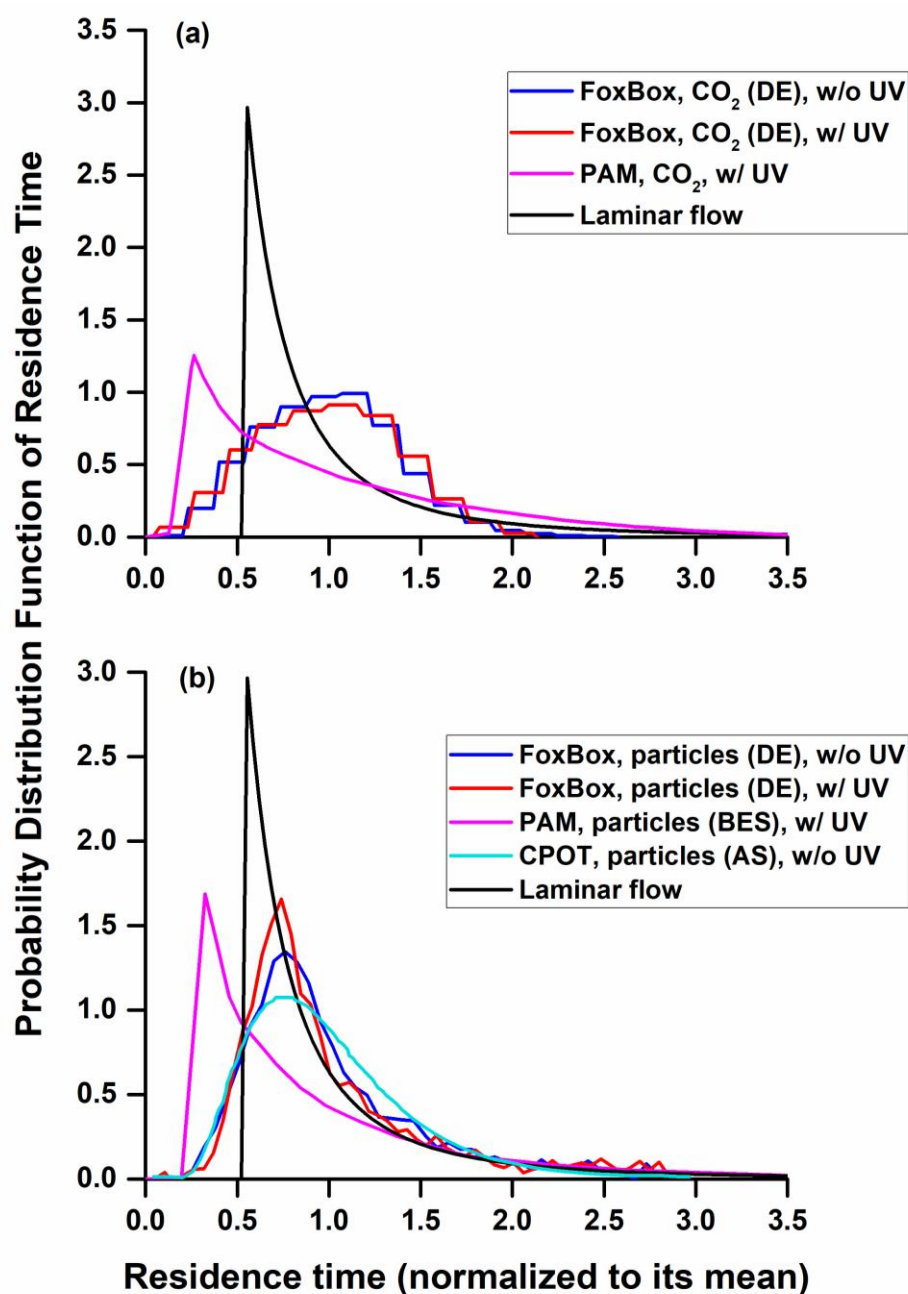


Fig. 3. Comparison of the probability density functions of residence times for the FoxBox (this study), PAM (Lambe et al. 2011), CPOT (Huang et al. 2017), and laminar flow (Huang et al. 2017), as a function of normalized residence time for: (a) CO₂, and (b) particles. Here, DE is diesel exhaust, AS is ammonium sulphate (AS), and BES is bis(2-ethylhexyl) sebacate (BES) particles. The FoxBox comparison was performed for both UV on (w/ UV) and UV off (w/o UV) conditions.

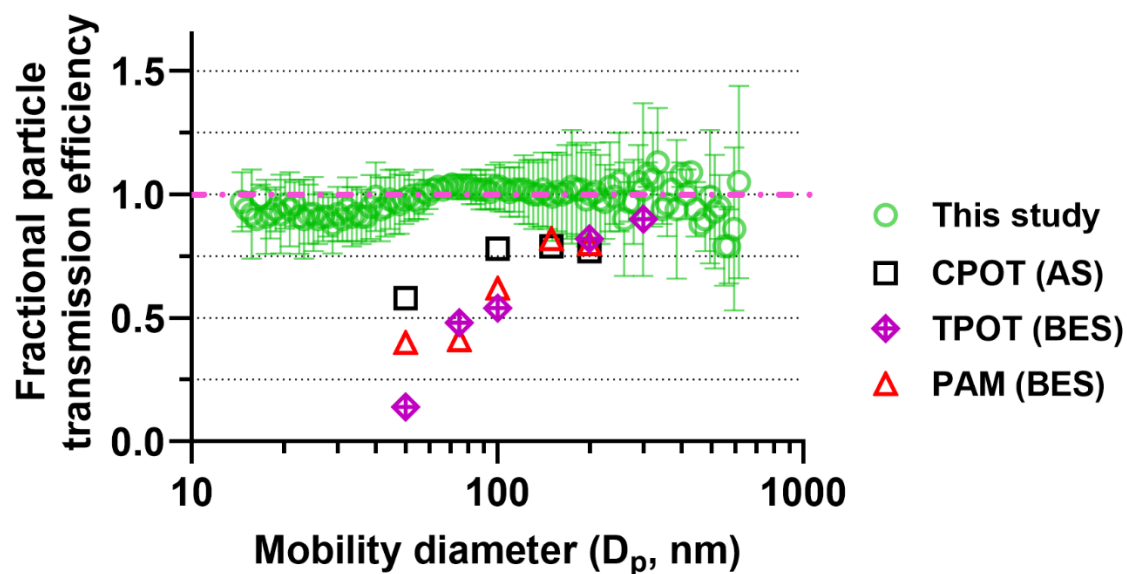


Fig. 4. Comparison of particle transmission efficiency of the FoxBox (this study) with CPOT (Huang et al. 2017), TPOT (Lambe et al. 2011) and PAM (Lambe et al. 2011) reactors. The particle transmission efficiency of the FoxBox was based on diesel exhaust (DE), CPOT on ammonium sulphate (AS), and TPOT and PAM on bis(2-ethylhexyl) sebacate (BES) particles. Error bars represent standard deviations. Pink dashed line corresponds to when all the particles are transmitted through the reactor.

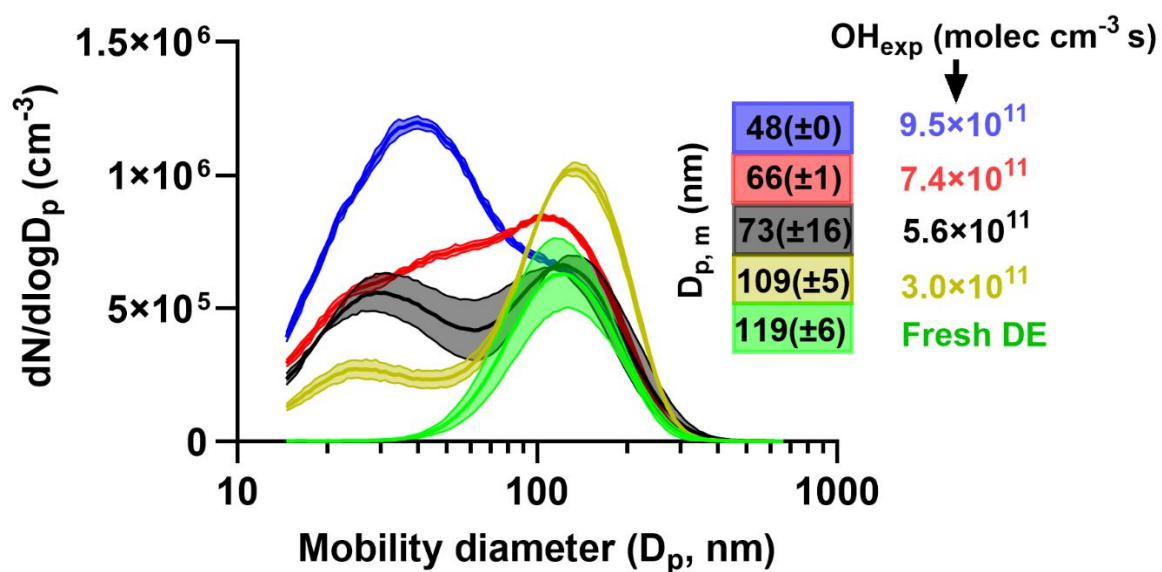


Fig. 5. Evolution in particle number size distribution ($dN/d\log D_p$) of DE as a function of OH exposure (OH_{exp}) during photochemical aging in the FoxBox. Here, $D_{p,m}$ represents median diameter \pm standard deviation.

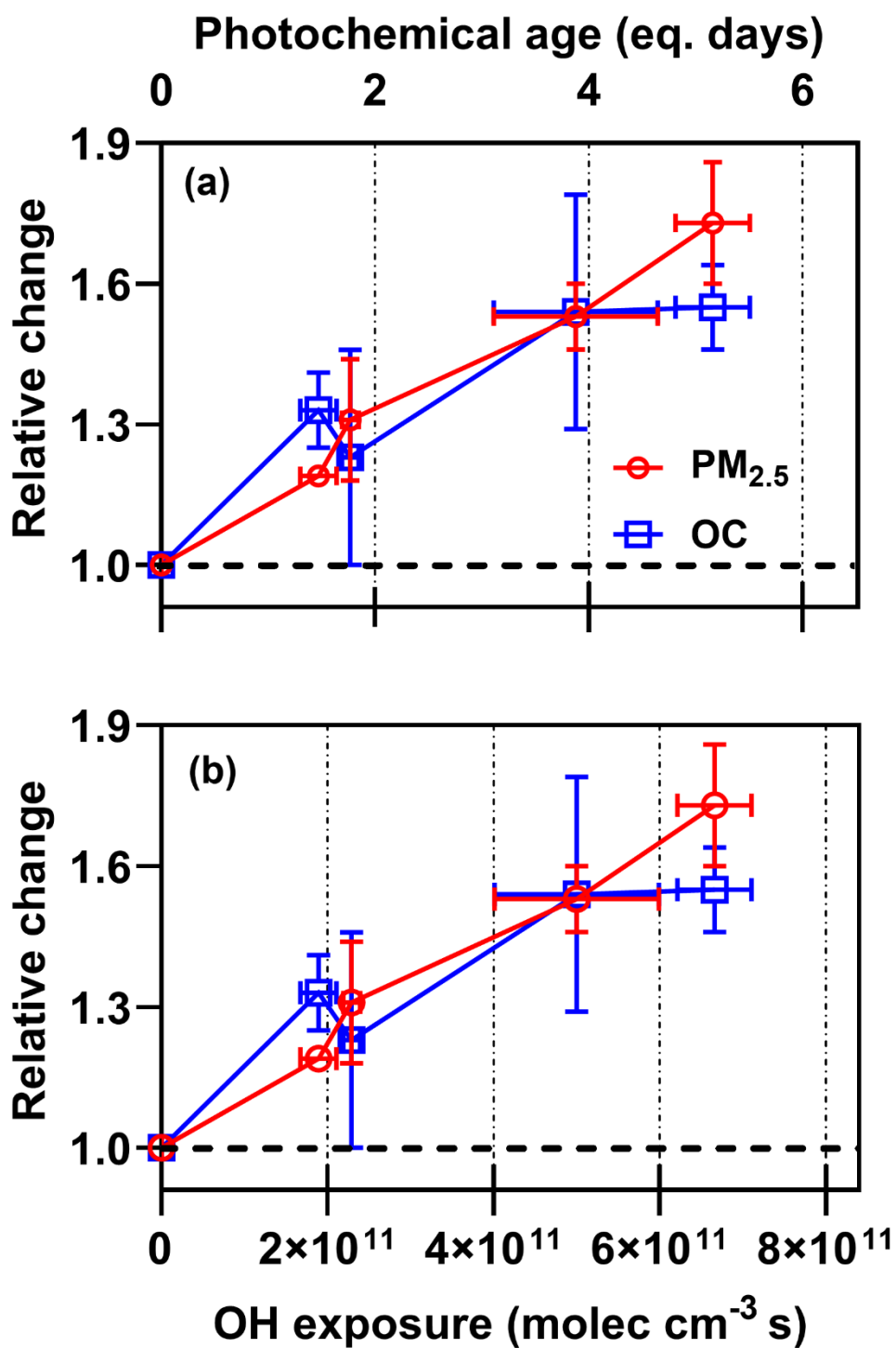


Fig. 6. Relative change in (a) PM_{2.5} and (b) organic carbon (OC) concentrations as a function of OH exposures and atmospheric equivalent photochemical age in the FoxBox. Error bars represent standard deviations.

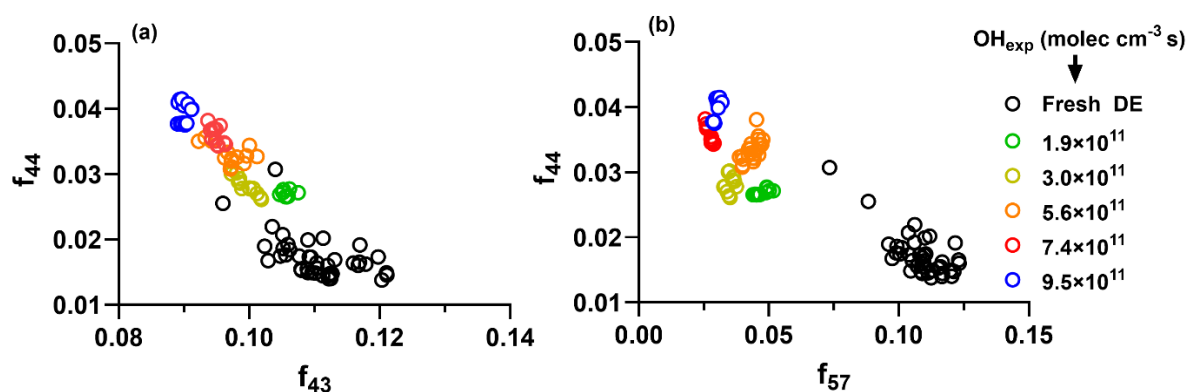


Fig. 7. Scatter plots of (a) f_{44} versus f_{43} , and (b) f_{44} versus f_{57} , for fresh and aged DE as a function of OH exposure (OH_{exp}) in the FoxBox. The f_{43} represents mainly C_3H_7^+ and $\text{C}_2\text{H}_3\text{O}^+$ fragments, f_{44} represents mainly CO_2^+ fragment and f_{57} represents mainly C_4H_9^+ and $\text{C}_3\text{H}_5\text{O}^+$ fragments. Higher f_{44} indicates greater oxidation of organic aerosols.

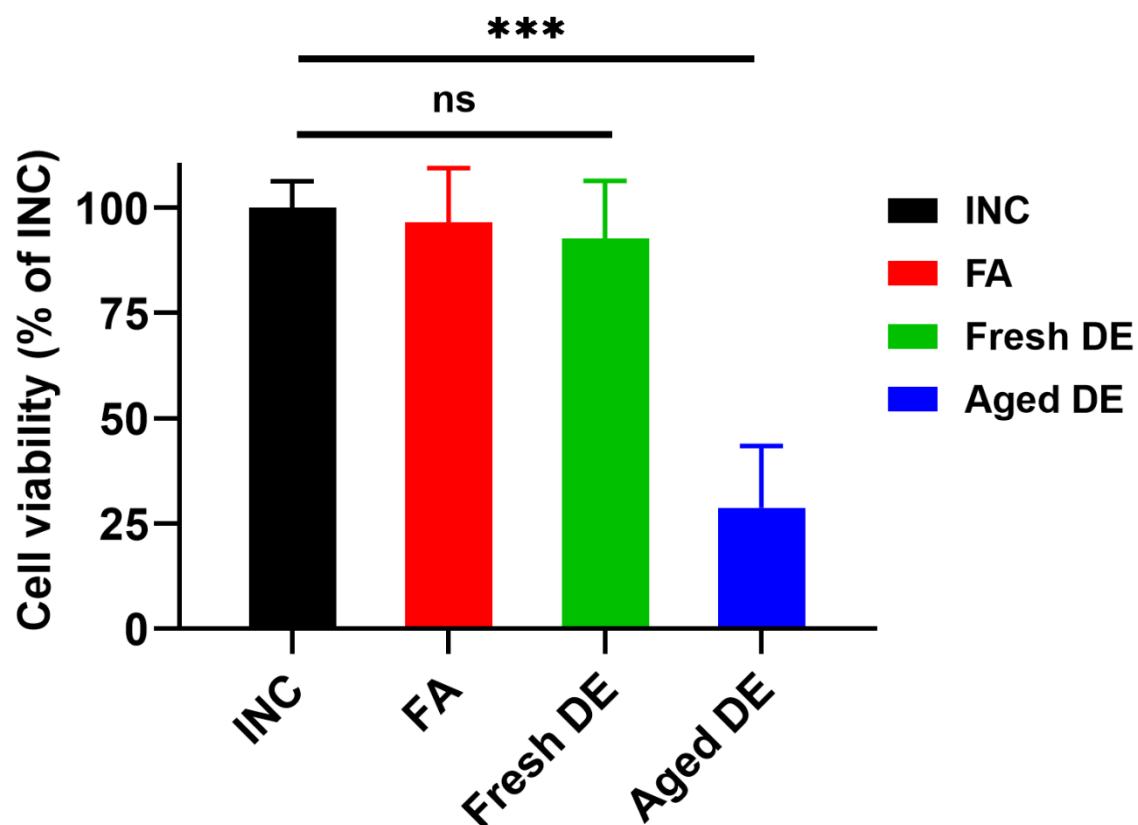


Fig. 8. Percent cell viability (relative to incubator control (INC)) of filtered air (FA), fresh and photochemically aged diesel exhaust (DE) at an OH_{exp} of $7.3 \times 10^{11} \text{ molec cm}^{-3} \text{ s}$ (atmospheric equivalent photochemical age: 5.7d). Error bars represent standard deviation in measurements.